The effects of a variation of the radial viscosity profile on mantle evolution

Uwe Walzer [a,*], Roland Hendel [a], John Baumgardner [b]

[a] *Institut für Geowissenschaften, Friedrich-Schiller-Universität, Burgweg 11, 07749 Jena, Germany*

[b] *Los Alamos National Laboratory, MS B216 T-3, Los Alamos, NM 87545, USA*

Abstract

The present paper describes a set of numerical experiments on the mantle's thermal evolution with an infinite Prandtl number fluid in a compressible spherical shell heated mainly from within. We used the anelastic liquid approximation with Earth-like material parameters. The usual variable-viscosity approach in mantle-convection models is the assumption of a temperature dependence only. The resulting thermal boundary layers are included in our model, too, but an additional viscosity profile of the interior mantle was derived: The Birch-Murnaghan equation was employed to derive the Grüneisen parameter and other physical quantities as a function of depth from observational values provided by PREM. We computed the melting temperature and a new mantle viscosity profile, called *eta3*, using the Grüneisen parameter, Lindemann's law and some solid-state physics considerations. The new features of *eta3* are a high-viscosity transition layer with rather high viscosity gradients at its boundaries, a second low-viscosity layer beginning under the 660-km discontinuity, and a strong viscosity increase in the central parts of the lower mantle. The rheology is Newtonian but it is supplemented by a viscoplastic yield stress, σ_y. A viscosity-level parameter, r_n, and σ_y have been varied. For a medium-sized Rayleigh-number–yield-stress area, *eta3* generates a stable, plate-tectonic behavior near the surface and simultaneously thin sheet-like downwellings in the depth. Outside this area three other types of solution were found. Not only the planforms but also the evolution of the Rayleigh number, the reciprocal Urey number, the Nusselt number, the surface heat flow, etc have been studied. We repeated this investigation with two very different basic viscosity profiles, *etaKL5a* and *etaKM* , of other authors. A comparison reveals that *eta3* facilitates the generation of surface plates and thin sheet-like downwellings in the depth considerably more than *etaKL5a* or even *etaKM*: The presence of *two* internal low-viscosity layers is obviously conducive for plateness and thin sheet-like downwellings. For an infinite yield stress, the thin cold sheet-like downwellings are reticularly connected. However, the distribution of the downwellings is more Earth-like if a realistic yield stress is added.

Key words: mantle convection, viscosity profile, melting temperature,

1 Introduction

In this paper, a compressible spherical-shell convection model of the Earth's mantle with decaying radiogenic heat sources has been investigated. Especially the long-time behavior of the system is interesting, to compare it with the mantle's evolution. For this comparison, not only the evolution of a few parameters as Rayleigh number, Urey number etc is relevant but also the general planforms of the flow, the distribution of the temperature, the plateness near the surface, the geometry of the downwellings, the spectra of temperature and creeping velocities as a function of time and depth, etc. Therefore, the success of a model depends on a variety of parameters. The core-mantle boundary (CMB) is assumed to be laterally isothermal at a particular time. Like other authors (Steinbach et al. 1993; Honda and Yuen, 1994; Yuen et al., 1995; Honda and Iwase, 1996) that have computed mantle convection calculations with decaying heat sources and an evolving CMB temperature, T_c, we implement a cooling core-mantle evolution model, i.e., we adjust T_c after each time step according to the heat transported from the core to the mantle. However, for comparison we used also runs with temporally constant T_c.

We derived a *new* viscosity profile, *eta3*, of the mantle from PREM (Dziewonski and Anderson, 1981) and mineral physics. The rheology has been varied not only by a viscosity-level parameter but also by a yield stress. By this twofold variation of parameters a multitude of runs has been generated, already for *eta3*. Each run gave a multitude of information that has been evaluated. The whole procedure has been repeated with two totally different viscosity profiles of other authors in order to discuss the mechanism. Other authors have already studied the influence of depth dependence of mantle viscosity, sometimes combined with temperature dependence (Christensen, 1984a; Gurnis and Davies, 1986; Balachandar at al., 1992; Hansen et al., 1993; Cserepes, 1993; Steinbach and Yuen, 1994; Bunge and Richards, 1996; Bunge et al., 1996, Tackley, 1996; Steinbach and Yuen, 1997; Cserepes and Yuen, 1997; Dumoulin et al., 1999; Cserepes et al., 2000). It is more suitable to discuss comparisons and details in Section 4 after the presentation of our results.

* Corresponding author.
  Email address: `u.walzer@uni-jena.de` (Uwe Walzer).

2 Model

2.1 Rheology

2.1.1 Focus of the paper

In the first place, we assume in this paper that bulk convection is based on Newtonian creep. According to Karato and Li (1992) and Li et al. (1996) this assumption is justified for the lower mantle, according to Karato and Wu (1993) also for the deep upper mantle. In the asthenosphere, Newtonian rheology should be a proper approximation for slow creeping processes at least. Furthermore we assume a viscoplastic yield stress, σ_y, for the uppermost 285 km. The yielding is implemented by an effective viscosity, η_{eff}, where

$$\eta_{eff} = \min[\eta(P,T), \frac{\sigma_y}{2\dot{\varepsilon}}] \tag{1}$$

In this formula, $\dot{\varepsilon}$ is the second invariant of the strain-rate tensor, P the pressure and T the temperature. The focus of this paper is, however, the pressure dependence of the viscosity and its effects on the convection and mantle evolution: Even if the lower mantle would be chemically homogeneous, the rise of activation enthalpy with pressure would generate an essential increase of viscosity. Moreover, it is to be expected that activation volume and activation energy jump at the three well-known phase boundaries of the transition layer. Only the direction of this jump is still disputed. However, the garnet-to-perovskite-plus-Al_2O_3 transition will cover a 50-100 km thick layer. The following is intended to explain the derivation of our viscosity profile. Our main objective is to be essentially independent on geochemical and detailed mineralogical assumptions. Furthermore, in *our* model we want to avoid such methods that derive the viscosity profile from geoid, free-air anomalies, seismic tomography and postglacial uplift since these methods yield a confusing multitude of contradictory models. From these investigations we use *for eta3* only the Haskell value of the asthenospheric viscosity in order to calibrate our profile.

2.1.2 Model of melting temperature

For each layer of the mantle separately, we search for a relation between the melting temperature, T_m, and the density ratio, x, with $x = \rho_0/\rho$ where ρ is the density and ρ_0 a reference density. This relation is important since the activation enthalpy of the viscosity law can be replaced by the product of a constant with the melting temperature. Lindemann (1910) proposed that melting takes place when the vibrations of the atoms exceed a certain threshold

that depends on the lattice. Based on this suggestion, Gilvarry (1956) derived a formula for isotropic monatomic crystals

$$\frac{\partial \ln T_m}{\partial \ln x} = 2 \left(\frac{1}{3} - \gamma\right) \left(1 + \gamma c_v \frac{\Delta V}{V} M\right) \tag{2}$$

where γ is the Grüneisen parameter, c_v the specific heat at constant volume, $\Delta V/V$ the relative volume change and M a constant that can be derived from the Debye-Waller formula. The second set of parentheses is virtually unity. Some authors derived modifications of this formula and enlarged the range of validity, e.g. Poirier (1986). Our starting point is PREM. In that model, the density, ρ, the pressure, P, the bulk modulus, K, and dK/dP have been derived as a function of the radius, r, from observations. Moreover, we use the third-order Birch-Murnaghan equation of state

$$P = \frac{3K_0}{2} \left(x^{-7/3} - x^{-5/3}\right) \left[1 + \frac{3}{4} \left(K_0' - 4\right) \left(x^{-2/3} - 1\right)\right] \tag{3}$$

and

$$K = -x \left(\partial P/\partial x\right)_T \tag{4}$$

and, according to Stacey (1996),

$$\gamma = \left[\frac{1}{2} \cdot \frac{dK}{dP} - \frac{1}{6} - \frac{1}{3} f \left(1 - \frac{1}{3} \cdot \frac{P}{K}\right)\right] / \left[1 - \frac{2}{3} f \frac{P}{K}\right] \tag{5}$$

We use $f = 2$ for closest packing to avoid a more complex mineralogical function, $f(r)$, based on debatable mineralogical assumptions. Smoothing over each layer of the mantle separately, the model values of the zero-pressure bulk moduli, K_0, the pressure derivative of the bulk modulus at vanishing pressure, K_0', $\rho(r)$, $K(r)$, $\gamma(r)$ and $T_m(r)$ were determined using Eqs. (2) to (5), PREM and a fixed value of T_m, e.g. we use $T_m = 2186K$ at 300 km depth (Ito and Takahashi, 1987; Thompson, 1992). Fig.1 shows that our melting curve as a function of the pressure is realistic. The intersection of $T_m(r)$ and the adiabat near the CMB point to the possibility of a very thin molten layer at the base of D". This issue has been discussed by several authors (Garnero and Helmberger, 1996; Steinbach and Yuen, 1999).

2.1.3 Model of viscosity

A full regard of the temperature dependence of the viscosity *as a variable* is numerically not feasible during the solution of the balance equations. There-fore, we put a part of the temperature dependence into a viscosity profile: We

determine the radial factor of the viscosity by replacing the temperature, T, in

$$\eta = \eta_0 \exp(k_2 T_m/T) \qquad (6)$$

by a mean adiabat, the T_m in Eq. (6) by $T_m(r)$ from Fig.1 and by equating $k_2 = 17$ for diffusion creep according to Karato et al. (2001). Moreover, the viscosity at 300 km depth is fixed to the Haskell (1935) value of 10^{21} Pa s. However this value was derived only as an average upper-mantle value (cf. Mitrovica, 1996). So we derive a radial factor of the viscosity labelled *eta2* in Fig.2. Since the thermal boundary layers at surface and CMB are incorporated in PREM, they are also a part of *eta2*.

The nature of viscosity in the transition layer is somewhat controversial, yet. Alternative models are discussed in Sections 3.3 and 4. For *our* model, the usual assumption was adopted that the downgoing slab is cooler than the surrounding. Therefore, the slab has a higher viscosity than the surrounding. If the cool slab penetrates a highly viscous layer on its way to the depth then high shear stress should be collected that can cause earthquakes in the short-period range. According to Kirby et al. (1996) and many other authors, the transition layer has a relative maximum of released earthquake energy as a function of depth. This conclusion will not be essentially modified if the cold slab in the deep transition zone is characterized by a weak, fine grained spinel region surrounded by narrow but strong regions (Karato et al., 2001). Already Ringwood (1990) emphasized that the garnet content in the transition layer grows with depth and that there are more than 90% garnet at the bottom of the transition layer. Independent of the correctness of the latter statement, Karato et al. (1995) derived a maximum of the viscosity of garnet, but also of the wadsleyite and ringwoodite for the transition zone with a jump to the lower viscosity of olivine of the asthenosphere and a considerable jump to the viscosity of perovskite of the lower mantle. Karato (1997) stressed that the normalized creep strength of garnet is an order of magnitude or more higher than that of olivine and perovskite for the expected T_m/T-regions. The most creeping experiments have been made in the power law creep regime. If the creep is diffusion-controlled then a difference in the diffusion coefficient of about 10^3 can be expected (Karato et al., 1995). It is highly probable that not only the seismic velocities but also activation energy, activation volume and preexponential factor of the relevant creeping mechanisms must jump at the phase boundaries that correspond to 410, 520 and 660 km standard depth. Ranalli (1998) excluded jumps that produce a low-viscosity layer in the transition zone. Micro-scale stress measurements of the 1000s strength show that the stress capacity of wadsleyite, ringwoodite and majorite-rich garnet are an order of magnitude higher than that of olivine and magnesiowüstite (Weidner et al., 2001). If MgO (mw) and not magnesioperovskite is responsible for the
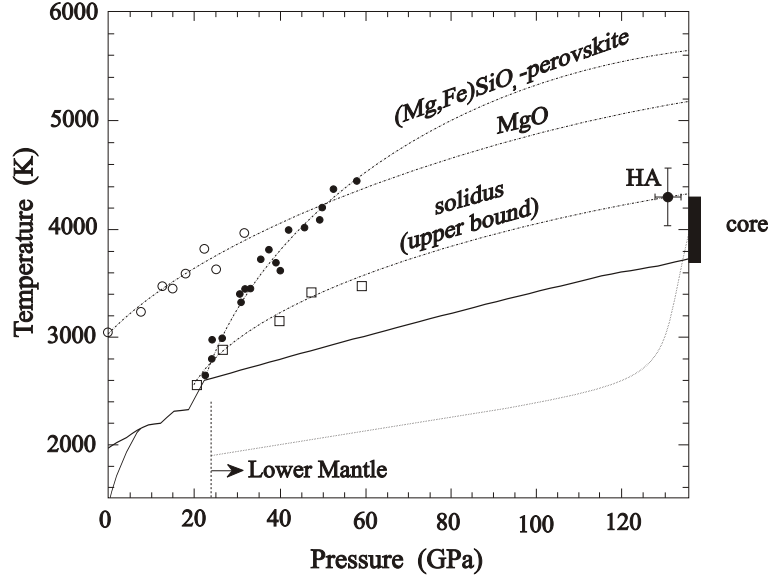
Fig. 1. A comparison of our melting curve (upper branch of the solid line) with curves given by Boehler (2000). The small lower branch are not computed by our algorithm but determined by experiments (Zhang and Herzberg, 1994; Zerr et al., 1998). The measured solidus temperatures (dash-dotted lines according to Zerr et al., 1998) are upper bounds for the relevant minerals. HA denotes an extraploation parallel to the MgO melting curve using Holland and Ahrens (1997). The dotted line represents the average geotherm that follows an adiabat.
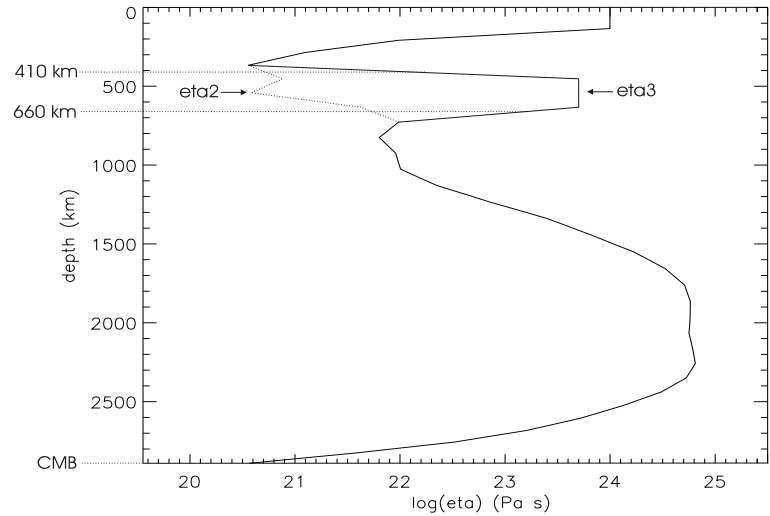

Fig. 2. The viscosity profiles η_2 and η_3. See text.

creeping behavior of the lower mantle then the paper of Weidner et al. (2001) could be a further hint to a high-viscosity transition layer. Based on results of the Karato group, Walzer et al. (2003) derived the viscosity profile *eta3* of Fig.2. It deviates from *eta2* only in the transition-layer region. Also a reduction of the grain size will probably contribute to the viscosity jump backward in 660 km standard depth. Using experiments, Yamazaki et al. (1996) studied the grain size for a two-phase system of perovskite and periclase. Based on grain-

growth experiments of this kind, Solomatov et al. (2002) found constraints from numerical modeling of grain growth and suggested that the grain size is very small after the phase deformation at 660 km depth. If the high-viscosity transition layer is justified in terms of the garnet-perovskite system, then the following should be taken into consideration. The most relevant reaction is garnet dissociating to $MgSiO_3$ and $CaMgSiO_3$ perovskites and Al_2O_3. This process begins at nearly the same pressure as in the olivine system, but the transition region is enlarged by 2-3 GPa or a 50-100 km depth range below the 660-km discontinuity (Irifune and Ringwood, 1987; Ito, 1989; Schubert et al., 2001) This is reflected in the steep negative gradient of *eta3* near and mainly beneath 660 km depth (See Fig.2). The thickness of the layer of viscosity decrease is in the mentioned order of magnitude.

In this paper, we use for the viscosity, η, the formula

$$\eta(r, \theta, \phi, t) = 10^{r_n} \cdot \eta_3(r) \cdot \exp\left[c_t \cdot T_m(r) \cdot \left(\frac{1}{T(r, \theta, \phi, t)} - \frac{1}{T_{av}(r, t)}\right)\right] \quad (7)$$

where T_{av} is the laterally averaged temperature, θ the colatitude, ϕ the longitude, t the time and c_t a constant. If we would put greater parts of the temperature dependence into the third factor of the right-hand side of Eq. (7) then the numerical problems prove to be insurmountable. The horizontally moving oceanic lithospheric plates cannot be generated by a viscous fluid with an Arrhenius law or by power-law rheology (Christensen, 1984b; Solomatov, 1995; Bercovici, 1998; Weinstein, 1998; Tackley, 1998; Trompert and Hansen, 1998; Monnereau and Quéré, 2001; Berovici et al., 2001). Shear localization and weakening seems to be important for the subduction mechanism. Since lithospheric strengths of somewhat more than 10^8 Pa are sufficient for supercontinents to break up (Gurnis, 1988; Lowman and Jarvis, 1999), we used a simple criterion for the introduction of yield stress into the lithosphere, namely Eq. (1), as Tackley (2000a) and Richards et al. (2001) did. The introduction of the factor 10^{r_n} is a generalization of Eq. (7). For our first estimate of the viscosity, $r_n = 0$ has been chosen. The variation of the non-dimensional parameter r_n generates a systematic shift of the viscosity level. In Section 3.3, we investigate the effects of totally different viscosity profiles of other authors on the evolution of the Earth's mantle.

2.2 Balance equations

The model is based on the numerical solution of the balance equations of energy, momentum and mass. From the well-known equation

$$\rho c_p \frac{dT}{dt} = \bigtriangledown \cdot (k \bigtriangledown T) + Q + \alpha T \frac{dP}{dt} + 2W_D \quad (8)$$

7

the following formula can be derived

$$\frac{\partial T}{\partial t} = -\frac{\partial(Tv_j)}{\partial x_j} - (\gamma - 1)T\frac{\partial v_j}{\partial x_j} + \frac{1}{\rho c_v}\left[\tau_{ik}\frac{\partial v_i}{\partial x_k} + \frac{\partial}{\partial x_j}\left(k\frac{\partial}{\partial x_j}T\right) + Q\right] \quad (9)$$

where Q is the heat generation rate per unit volume, x_j and v_j are the components of the location vector and the velocity, k is the thermal conductivity, c_p the specific heat at constant pressure, W_D is viscous dissipation and compressional heat generation rate per unit volume, α the coefficient of thermal expansion. Thus we have an alternative expression for the *energy conservation*. Although c_v appears in Eq. (9), the latter is equivalent to Eq. (8) where c_p is used. The deviatoric stress tensor can be expressed by

$$\tau_{ik} = \eta\left(\frac{\partial v_i}{\partial x_k} + \frac{\partial v_k}{\partial x_i} - \frac{2}{3}\frac{\partial v_j}{\partial x_j}\delta_{ik}\right) \quad (10)$$

in Eq. (9) where η is the viscosity. For the *equation of state* we choose

$$\rho = \rho_r\left[1 - \alpha(T - T_r) + K_T^{-1}(P - P_r) + \sum_{k=1}^{2}\Gamma_k\Delta\rho_k/\rho_r\right] \quad (11)$$

where the index r refers to the adiabatic reference state, $\Delta\rho_k/\rho_r$ or f_{ak} (see Table 1) denotes the non-dimensional density jump for the kth phase transition. Γ_k is a measure of the relative fraction of the heavier phase where $\Gamma_k = \frac{1}{2}\left(1 + \tanh\frac{\pi_k}{d_k}\right)$ with $\pi_k = P - P_{0k} - \gamma_k T$ describing the excess pressure π_k. The quantity P_{0k} is the transition pressure for vanishing temperature T. A non-dimensional transition width is denoted by d_k (see Table 1). γ_k (see Table 1) represents the Clapeyron slope for the kth phase transition. Γ_k and π_k have been introduced by Richter (1973) and Christensen and Yuen (1985). K_T is the isothermal bulk modulus. Because of the very high Prandtl number, we have the following version of the equation of *conservation of momentum*:

$$0 = -\frac{\partial}{\partial x_i}(P - P_r) + (\rho - \rho_r)g_i(r) + \frac{\partial}{\partial x_k}\tau_{ik} \quad (12)$$

where g_i denotes the components of gravity acceleration. The *conservation of mass* is expressed by

$$0 = \frac{\partial}{\partial x_j}\rho v_j \quad (13)$$

The Equations (9), (11), (12) and (13) are a system of six scalar equations we use to determine six scalar unknown functions, namely T, ρ, P and the three

Table 1
Model parameters

Parameter	Description	Value	
r_{min}	Inner radius of spherical shell	3.480×10^6	m
r_{max}	Outer radius of spherical shell	6.371×10^6	m
	Temperature at the outer shell boundary	288	K
γ_1	Clapeyron slope for the olivine-spinel transition	$+1.6 \times 10^6$	Pa·K^{-1}
γ_2	Clapeyron slope for the spinel-perovskite transition	-2.5×10^6	Pa·K^{-1}
f_{a1}	Non-dimensional density jump for the olivine-spinel transition	0.0547	
f_{a2}	Non-dimensional density jump for the spinel-perovskite transition	0.0848	
	Begin of the thermal evolution of the Earth's silicate mantle	4.490×10^9	a
d_1	Non-dimensional transition width for the olivine-spinel transition	0.05	
d_2	Non-dimensional transition width for the spinel-perovskite transition	0.05	
	Begin of the radioactive decay	4.565×10^9	a
c_t	Factor of the lateral viscosity variation	1	
k	Thermal conductivity	12	W·m^{-1}·K-1
$nr + 1$	Number of radial levels	33	
	Number of grid points	1.351746×10^6	
$a_{\mu\nu}(U)$	Concentration of uranium	0.0203	ppm
$a_{\mu\nu}(Th)$	Concentration of thorium	0.0853	ppm
$a_{\mu\nu}(K)$	Concentration of potassium	250	ppm

components of v_i. For a more detailed derivation of the basic equations, see e.g. Narasimhan (1993), Schubert et al. (2001) and Walzer at al. (2003).

2.3 Heating, initial and boundary conditions

Walzer and Hendel (1999) computed thermal mantle convection and chemical segregation together in a 2-D model where the generation of the depleted mantle and the growth of the continental crust were obtained as a function of time. In the present paper, however, we confine ourselves to the *thermal* evolution problem alone: the silicate mantle is homogeneously heated from within and also from the CMB. It is assumed that the concentrations, $a_{\mu\nu}$, of the radioactive elements of the primordial mantle according to McCulloch and Bennett (1994) determine the internal heating (Cf. Table 1). The time-dependent specific heat production, H, is computed from

$$H = \sum_{\nu=1}^{4} a_{\mu\nu} a_{if\nu} H_{0\nu} \exp(-t/\tau_\nu) \tag{14}$$

where τ_ν denotes the decay time or the $1/e$ life, $H_{0\nu}$ the initial heat generation rate per unit volume of the νth radionuclide, $a_{if\nu}$ the isotopic abundance factor, ν the indices of the four major heat-producing elements. The numerical values we use are listed in Table 2. The heat production rate per unit volume, Q, introduced in Section 3.2, is given by $Q = H \cdot \rho$.

We assume free-slip and impermeable boundary conditions for both the Earth's surface and the CMB. What about the thermal boundary conditions? The surface temperature is supposed to be constant (Cf. Table 1). In this paper, the CMB is isothermal as a function of the location vector at a particular time. As other researchers (e.g. Steinbach et al. 1993; Steinbach and Yuen, 1994; Honda and Iwase 1996) have done when implementing cooling core-mantle evolution models, we adjust the CMB temperature, T_c, after each time step according to the heat flow through the CMB. We took into consideration core cooling induced by mantle convection under the influence of Steinbach et al.(1993). The assumption is a homogeneous core in thermodynamic equilibrium. The equation of the cooling of the core is

$$\frac{d\Delta T}{dt} = -\frac{3\rho_m c_m h}{\rho_c c_c r_c} Nu(t) \cdot \Delta T(t) \tag{15}$$

where h is the depth of the mantle, $h = 2.891 \times 10^6$ m, c_m is the average specific heat of the mantle, averaged over our described curve, ρ_m, the mean mantle density was computed from PREM, r_c is the core radius with $r_c = $

10

Table 2
Data on major heat-producing isotopes

Isotope	$^{40}\mathrm{K}$	$^{232}\mathrm{Th}$	$^{235}\mathrm{U}$	$^{238}\mathrm{U}$
ν	1	2	3	4
$\tau_\nu[\mathrm{Ma}]$	2015.3	20212.2	1015.4	6446.2
$H_{0\nu}[\mathrm{Wkg}^{-1}]$	0.272×10^{-3}	0.0330×10^{-3}	47.89×10^{-3}	0.1905×10^{-3}
$a_{if\nu}$	0.000119	1	0.0071	0.9928

3.480×10^6 m, $c_c = 5 \times 10^2$ $\frac{J}{kg\ K}$ is the average specific heat of the core, $\rho_c = 1100$ $\frac{kg}{m^3}$ is the mean density of the core. The Nusselt number, Nu, was computed using the temperature difference across the mantle. Only for comparison, we did some runs with temporally constant T_c (See Section 3.4).

2.4 Numerical method and implementation

The solutions of the system of differential equations of convection in a compressional spherical shell, Eqs. (9) to (13) with the additional Eqs. (1), (7), (14) and (15), are obtained using a three-dimensional finite-element discretization, a fast multigrid solver and the second-order Runge-Kutta procedure. The mesh is generated by projection of a regular icosahedron onto a sphere to divide the spherical surface into twenty spherical triangles or ten spherical diamonds. A dyadic mesh refinement procedure connects the midpoints of each side of a triangle with a great circle such that each triangle is subdivided into four smaller triangles. Successive grid refinements generate an almost uniform triangular discretization of the spherical surface of the desired resolution. Corresponding mesh points of spherical surfaces at different depths are connected by radial lines. The radial distribution of the different spherical-surface triangular networks is so that the volumes of the cells are nearly equal. More details are given by Baumgardner (1983, 1985), Bunge et al. (1997) and Yang (1997). For the multitude of runs we needed for our parameter study, we employed a mesh with 1351746 nodes. Some runs were made with 10649730 nodes to check the convergence of the lower resolution runs. The result is that the laterally averaged heat flow, the ratio of heat outflow to radiogenic heat production, the Rayleigh number, and the Nusselt number as functions of the time show hardly any discernable differences (< 0.5 %). Calculations were performed on 128 processors of a Cray T3E. A scalability test showed a scaling degree of nearly 90 %. The code was benchmarked for constant viscosity convection by Bunge et al. (1997) with numerical results of Glatzmaier (1988) for Nusselt numbers, peak temperatures, and peak velocities. A good agreement (≤ 1.5 %) was found.

3 Results

3.1 *Plate-like motion near the surface and thin cold sheet-like downwellings*

Before the parameter variation of the present model is shown and before the effects of viscosity profiles of other authors on the thermal evolution is presented, we will describe the numerical results of our reference model with $r_n = 0$ and $\sigma_y = 1.35 \times 10^8 Pa$. We anticipate that the main features of this solution, especially of the planforms, apply also for a wider range of Rayleigh numbers, Ra_H, and yield stress, σ_y. The laterally averaged temperature, T_{av}, as a function of depth for the geological present is shown in Fig.3. T_{av} is not far from the geotherm of whole-mantle convection by Schubert et al. (2001). Also the planforms show that our model is nearer to whole-mantle convection than to layered convection. *Our* thermal CMB condition is determined by the cooling core. However, if we fix the CMB temperature with respect to time then the temperature profile is increased in comparison to the reference curve. This result applies also for runs with other Ra_H and σ_y. Although it is certainly true that the CMB is laterally isothermal at a particular time, T_c has decreased with time since we know from observations that the mantle is cooling. Therefore for *evolution* models, the temperature difference, ΔT between lower and upper boundary cannot be a constant. However, for convection models for some 100 Ma the assumption $\Delta T = const$ is acceptable.

An essential result of this paper is the *viscosity profile.* This profile is somewhat variable as a function of time. Fig.4 shows the laterally averaged viscosity as a function of depth for the geological present. By numerical improvements, we are now able to transfer the viscosity jumps at 410 and 660 km depth considerably better into the model. The jump in the kind of lattices at the phase transition generates jumps in activation volume, activation energy and preexponential factor and therefore viscosity jumps. The gradual viscosity increase in the lower mantle depends, however, on the product of activation volume times rising pressure: The rising pressure diminishes not only the number of defects per unit volume, but also the energy required to jump from one site to another increases with pressure. The strong decrease of viscosity immediately above the CMB is induced by a strong temperature rise in D". The latter viscosity decrease is described mainly by $\eta_3(r)$. For numerical reasons, only a small part of this decrease is in the third factor of the right-hand side of Eq. (7).

The first panel of Fig.5 shows the laterally averaged heat flow at the Earth's surface as a function of time in the past. We obtain the right order of magnitude. The second panel represents the reciprocal Urey number, *Ror*. This
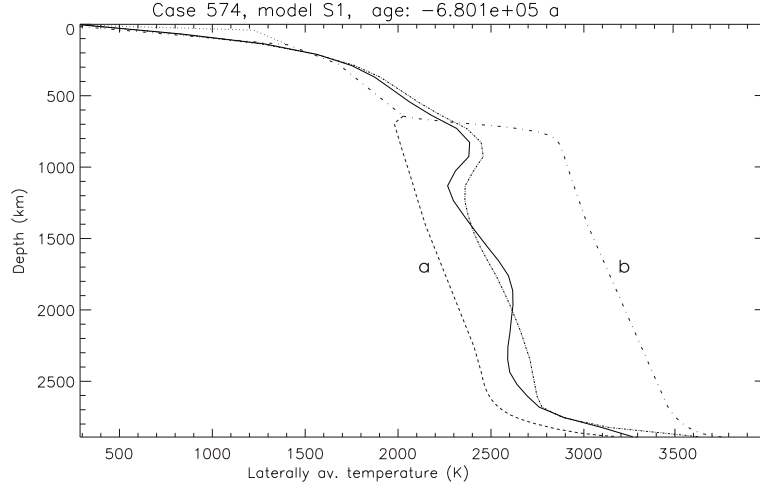
Fig. 3. The solid curve denotes the laterally averaged temperature of the geological present for the reference run with $\sigma_y = 135 MPa$. For this case, the CMB temperature, T_c, is spacially constant but variable in time according to the heat balance of the core. By way of exception, T_c is temporally averaged for this run and the run is repeated with this temporally averaged T_c as a temporally constant thermal boundary condition. The resulting laterally averaged temperature for the present as a function of depth is given by short dashes. It is in general somewhat higher than the usual temperature profile. The range of possible mantle geotherms according to Schubert et al. (2001) is shown for comparison. Label a and b denote geotherms of whole-mantle and partially layered convection, respectively. The dotted line corresponds to the ridge geotherm.
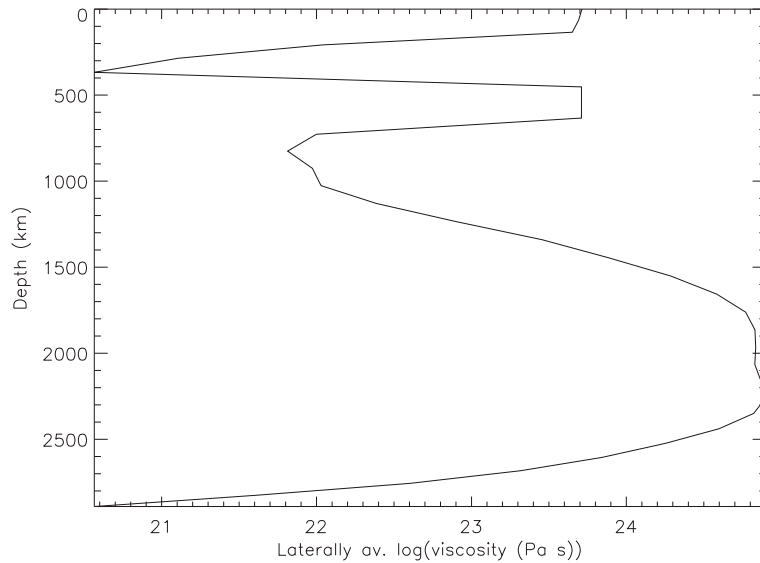

Fig. 4. The laterally averaged viscosity of the reference run for the geological present.

quantity rises slightly undulating as a function of time, i.e., in spite of persistent radioactive heating from within, the internal energy of the mantle decreases. The temporal average of the reciprocal Urey number, $\overline{Ror}$, of this reference run is 1.518. The estimates of this number for the Earth are some-
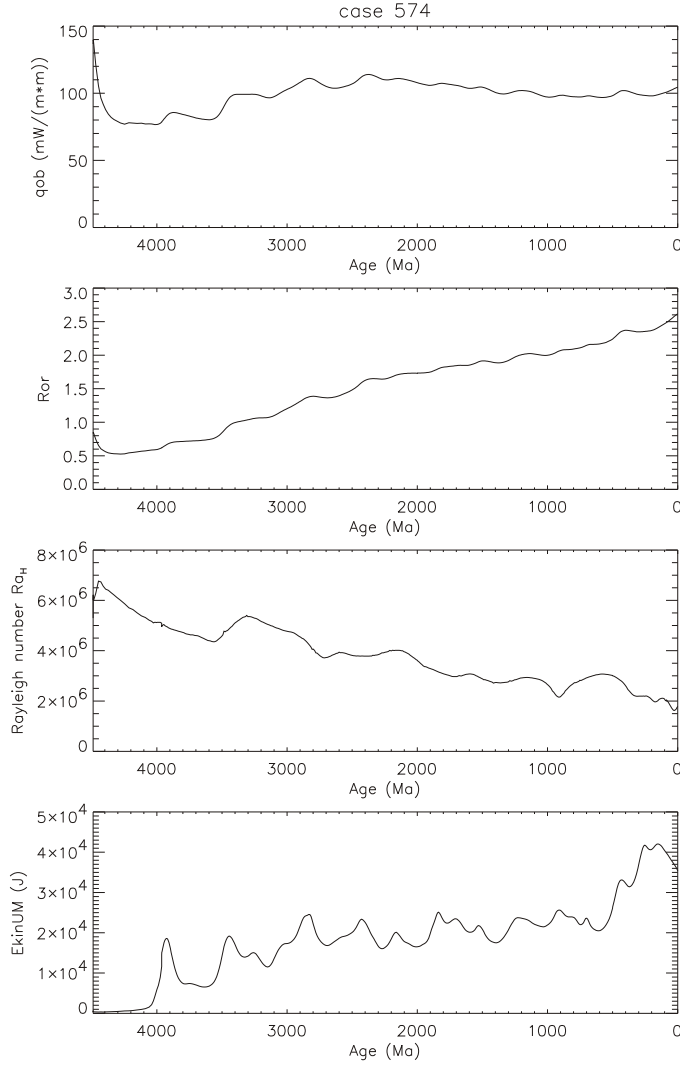
13

Fig. 5. The evolution of the laterally averaged surface heat flow, *qob*, of the ratio of surface heat outflow per unit time to the mantle's radiogenic heat production per unit time, *Ror*, of the Rayleigh number, Ra_H, and of the kinetic energy of the thermal convection in the upper mantle, $E_{kin,UM}$.

what different. Stacey and Stacey (1999) derived a somewhat high value of 1.85, whereas Schubert et al. (2001, p. 648) give the same possible interval, namely $1.25 < \overline{Ror} < 1.67$, for Earth and Venus. The third panel of Fig.5 shows the time history of the Rayleigh number, Ra_H, that is defined by

$$Ra_H = \left\langle \frac{\rho \alpha g h^3}{\kappa \eta_{al}} \cdot \frac{(Qh + q_c)\,h}{k} \right\rangle \tag{16}$$

where q_c is the heat flow at the CMB and κ the thermal diffusivity. The quantity η_{al} is given by
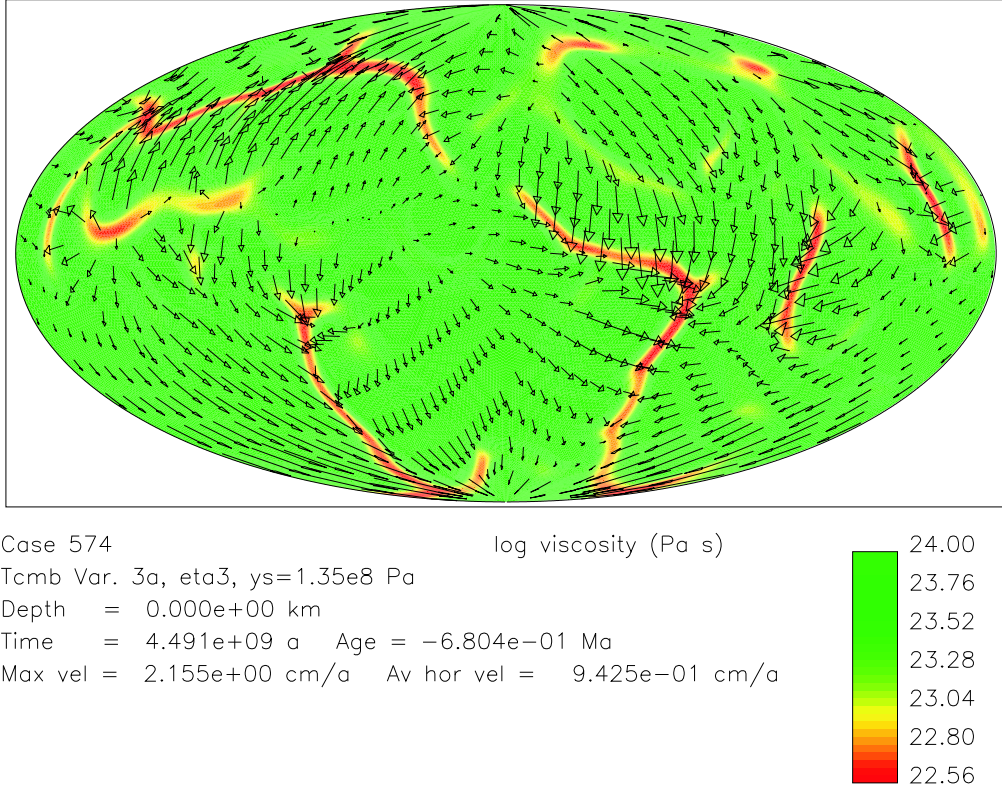
$$\log \eta_{al} = \langle \log \eta \rangle \tag{17}$$

14

Case 574   log viscosity (Pa s)   24.00
Tcmb Var. 3a, eta3, ys=1.35e8 Pa   23.76
Depth   =   0.000e+00 km   23.52
Time   =   4.491e+09 a   Age = −6.804e−01 Ma   23.28
Max vel =   2.155e+00 cm/a   Av hor vel =   9.425e−01 cm/a   23.04
                                                                          22.80
                                                                          22.56

Fig. 6. Equal-area projection with the surface distribution of log viscosity (colors) for yield stress of $135MPa$. The creeping velocities (arrows) show a plate-like distribution. Elongated high strain rate zones have reduced viscosity due to plastic yielding. Fig.10 shows that there is a greater range of Rayleigh numbers, Ra_H, and yield stresses, σ_y, with such a kind of solutions.

The bracket $\langle \rangle$ denotes a volumetric average but not a temporal average. Since Q, q_c and η_{al} are functions of the time, Ra_H is also a temporal function. The fourth panel of Fig.5 displays the kinetic energy of upper-mantle convection. This could possibly be a measure for the orogenetic activity. However, the position of the maxima is partly different for different runs produced by variation of the parameters. (See Section 3.2). Only the frequency content and the general behavior of the curve stay similar.

Fig.6 presents the surface planform of our 3-D spherical calculation with a yield stress of 135 MPa. Colors signify the viscosity, arrows stand for the creeping velocity. We obtain *plate-like* areas with nearly constant angular velocity around the center of the Earth, constant within each "plate". Especially the directions are very persistant within each "plate". Subduction zones and spreading zones have reduced viscosity. They are shown in red and yellow colors in Fig.6. In corresponding runs without yield stress, that is not shown here, we obtained a reticulated network of thin tabular-shaped downwellings. They are thinner than those in other publications. This is evidently a consequence of our viscosity profile with two interior low-viscosity zones, i.e., for other

15

Case 574
Tcmb Var.3a eta3 ys=1.35e8 Pa
Depth   =   6.329e+02 km
Time   =   4.491e+09 a   Age = −6.804e−01 Ma
Max vel =   1.533e+00 cm/a   Av hor vel =   3.034e−01 cm/a

Temperature
(K)

3844.
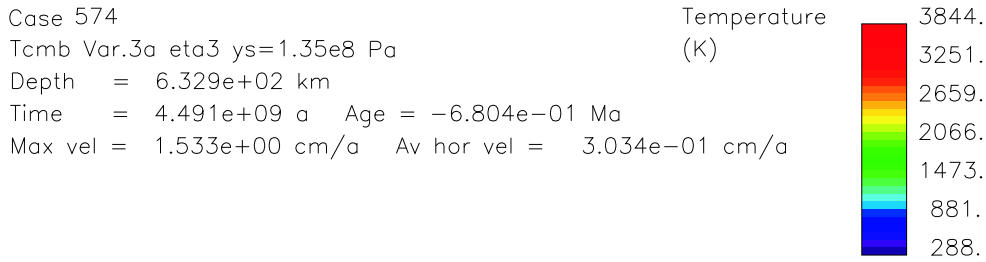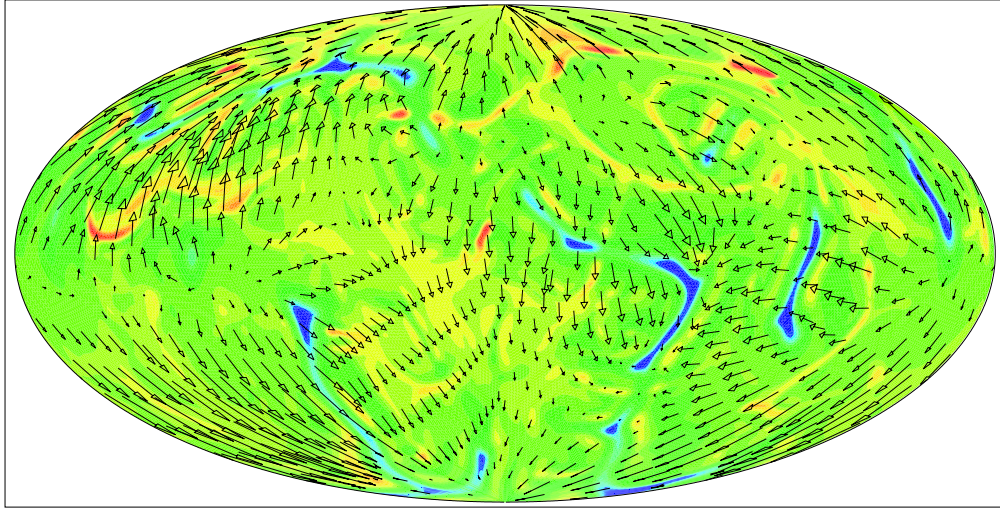3251.
2659.
2066.
1473.
881.
288.

Fig. 7. Equal-area projection of the temperature distribution (colors) and the creeping velocities (arrows) of our reference run for the geological present and for 632.9 km depth. $\sigma_y = 135 MPa$. The blue downwelling zones can be pursued in other equal-area projections up to the surface where the convergent zones of reduced viscosity are situated in Fig.6.

profiles the tabular-shaped downwellings are also present but less thin. For runs with vanishing yield stress, however, the network is too close-meshed in comparison with the real Earth. For runs with moderate σ_y and Ra_H around our reference run of Fig.6, we obtain a smaller number of subducting-slab-like downwellings. Their number and distribution is Earth-like. Fig.7 shows the temperature distribution (color) and the creeping velocity (arrows) for the same run and the same age but in 632.9 km depth. The elongated cold tabular-shaped downwellings of Fig.6 are visible in Fig.7 at blue lines at the same place. The slab-like features cross the high-viscosity transition layer. They are only partly joined with each other as the slabs of the real Earth. In contrast with the real Earth the downwellings of the model descent perpendicularly. The physical process connected with the slab dip of the subduction is somewhat enigmatic, yet, but there seems to be a connection with the neighboring continent. So, this feature of the model is not in the least surprising since it is true that the present model develops plates near the surface but it contains no continents. Also for other neighboring values of the yield stress and the Rayleigh number and for other ages, the model develops plates at the surface (See Fig.10). E.g., Fig.8 displays a plate-like behavior at the surface
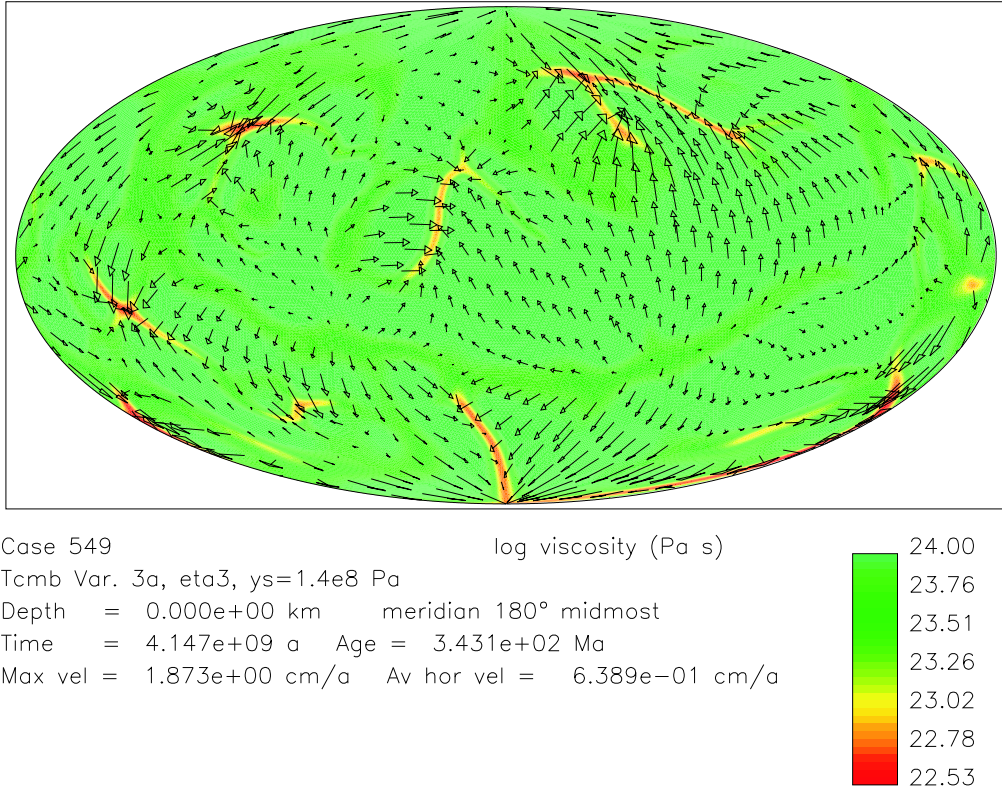
16

Case 549   log viscosity (Pa s)   24.00
Tcmb Var. 3a, eta3, ys=1.4e8 Pa   23.76
Depth   = 0.000e+00 km   meridian 180° midmost   23.51
Time   = 4.147e+09 a   Age = 3.431e+02 Ma   23.26
Max vel = 1.873e+00 cm/a   Av hor vel =   6.389e−01 cm/a   23.02
                                                                          22.78
                                                                          22.53

Fig. 8. Equal-area projection with the surface distribution of log viscosity (colors) and creeping velocities (arrows) for a yield stress $\sigma_y = 140 MPa$ and an age of 343 Ma.

for a run with a yield stress of 140 MPa and for an age of 343 Ma. The distribution of the plates has greatly changed since the age of 2000 Ma for the same run. (Cf. Fig.9). A few subduction zones have a similar location as for 343 Ma. But the most downwelling lines show a totally other position. Especially the directions of the plate-like motions near the surface have totally changed.

3.2   Variation of parameters

Fig.10 represents the character of the upper boundary layer and of the downwellings in the present model with *eta3* in a yield-stress–Rayleigh-number plot. The solid line surrounds a greater area with stable, plate-like behavior in the lithospheric region where thin sheet-like downwellings appear at the same time in the depth. The downwellings do not form a close-meshed network as in our models with infinite yield stress that are not shown here but they form loose chains as the subducting slabs of the real Earth. However, the downwellings of the model go down perpendiculary. Outside the solid line, the solutions of the model are subdivided into three types (See caption of Fig.10 and Section B.1.4). Tackley (2000a) describes convection models without essential pressure dependence of the viscosity and with Cartesian geometry. In his model with
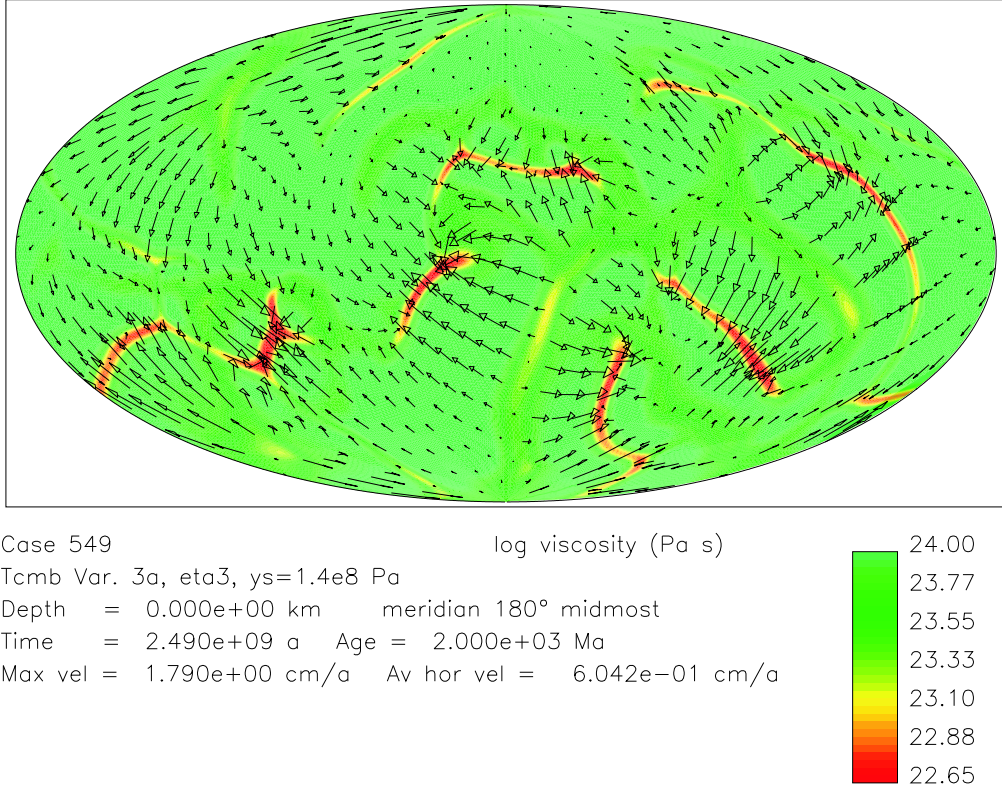
Case 549   log viscosity (Pa s)   24.00
Tcmb Var. 3a, eta3, ys=1.4e8 Pa   23.77
Depth   = 0.000e+00 km   meridian 180° midmost   23.55
Time   = 2.490e+09 a   Age = 2.000e+03 Ma   23.33
Max vel = 1.790e+00 cm/a   Av hor vel =   6.042e-01 cm/a   23.10
                                                                                    22.88
                                                                                    22.65

Fig. 9. Equal-area projection with the surface distribution of log viscosity (colors) and creeping velocities (arrows) for a yield stress $\sigma_y = 140 MPa$ and an age of 2000 Ma.

temperature-dependent viscosity, a mobile upper boundary is a consequence of a lower yield stress, σ_y, erratic mobility with incomplete plate boundaries arises from moderate σ_y and a stagnant lid emerges from very high σ_y (See also Solomatov, 1995). In Tackley's and also in our model, it is applicable that the effective viscosity in the upper boundary layer is determined by yielding rather than by the real physical temperature dependence of viscosity. Therefore, it is not only necessary for numerical reasons but it is also justifiable from the physical point of view that the greater part of the upper boundary layer is incorporated in $\eta_3(r)$ instead of the third factor of the right-hand side of Eq.(7).

Because of Eqs. (7) and (16), the special Rayleigh number, $Ra_H(2)$, decreases with rising viscosity-level parameter. This is to be seen in Fig.11. The monotonously falling function $Ra_H(2)(r_n)$ is evidently nearly independent of the yield stress. Especially the numerous runs with $r_n = 0$ show a nearly constant $Ra_H(2)$. Due to the weak temperature dependence of viscosity, Ra_H is determined mostly by the derived viscosity profile. Yielding affects only a small fraction of the mantle volume. Therefore, σ_y will not noticeably affect the mean viscosity. However, Fig.12 demonstrates that the temporal average of the ratio of surface heat outflow per unit time to the mantle's radiogenic heat
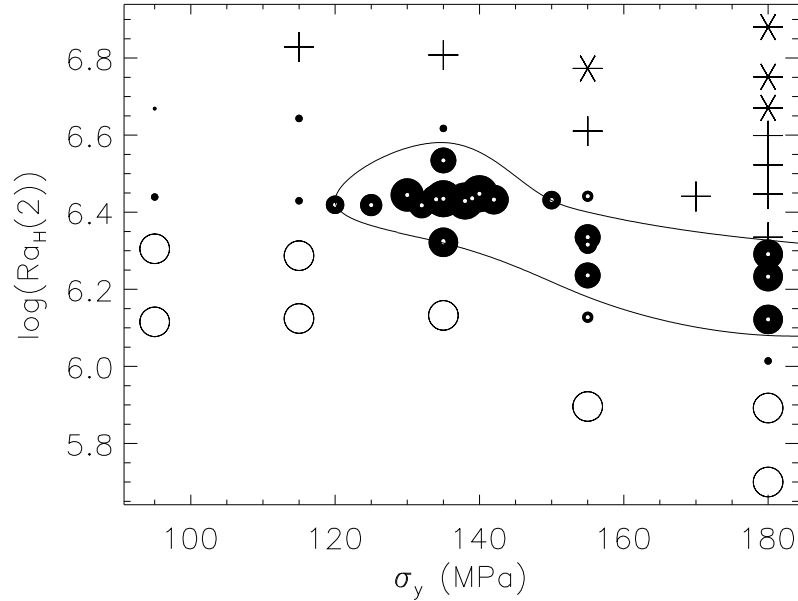
18

Fig. 10. The character of the solutions as a function of a Rayleigh number, $Ra_H(2)$, and the yield stress, σ_y. $Ra_H(2)$ is the temporal average of Ra_H over the last 2000 Ma. Little black disks with white center stand for runs with plate-like movements along the surface that show plate-like thin downwelling sheets, too. The radius of the disk is a measure of plateness near the surface. White circles represent runs without plates near the surface that have a wide-meshed network of broad downwelling zones. For this type of solution, the maximum of the T_l^{rms}-spectrum is shifted toward small spherical harmonic degrees, l. Plus signs denote runs without plates near the surface that show a diffuse disintegration of the network of cold areas near the surface. In the depth of some hundred kilometers, there are a few isolated thin elongated slab-like downwellings. For all depths, there is a relatively broad T_l^{rms}-spectrum for this type of solution. Therefore, the corresponding equal-area projections with the temperature distribution are rather rich in details and has a fine structure. Asterisks stand for runs without surface plates and without slab-like downwellings in the mantle as well. They show very broad T_l^{rms}-spectra.

production per unit time over the last 2000 Ma, $Ror(2)$, depends on r_n as well as on σ_y. At high yield stress, $Ror(2)$ increases with rising r_n. At constant r_n, $Ror(2)$ ascends with decreasing yield stress, i.e., the upper boundary layer will be plastically deformed the earlier, the lower the yield stress is. This breaking up facilitates the heat emission whereas the radioactive decay is entirely unaffected. Fig.13 displays that the special Nusselt number, $Nu(2)$, depends on r_n as well as on σ_y.
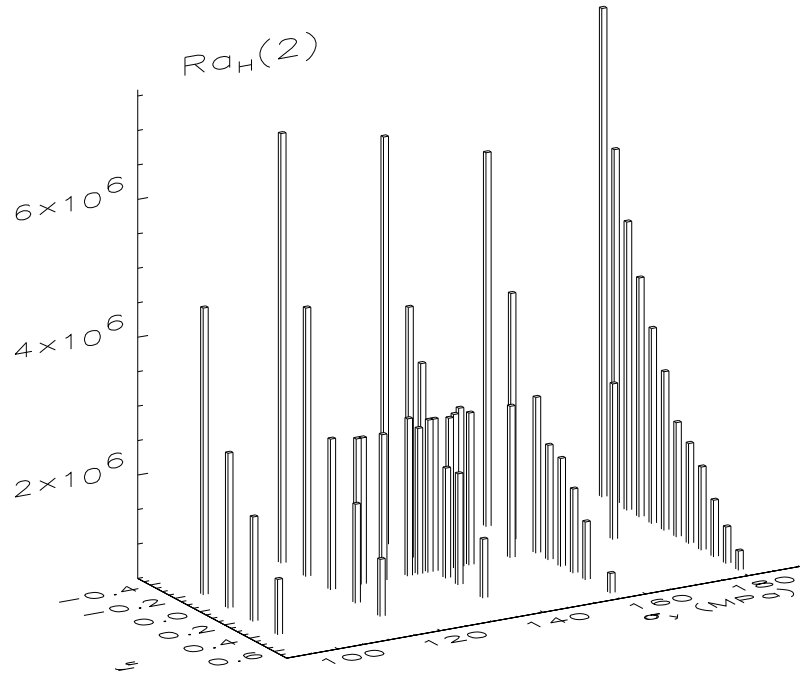
19

Fig. 11. $Ra_H(2)$ as a function of σ_y and the viscosity-level parameter, r_n. Further explanations see Fig.10.
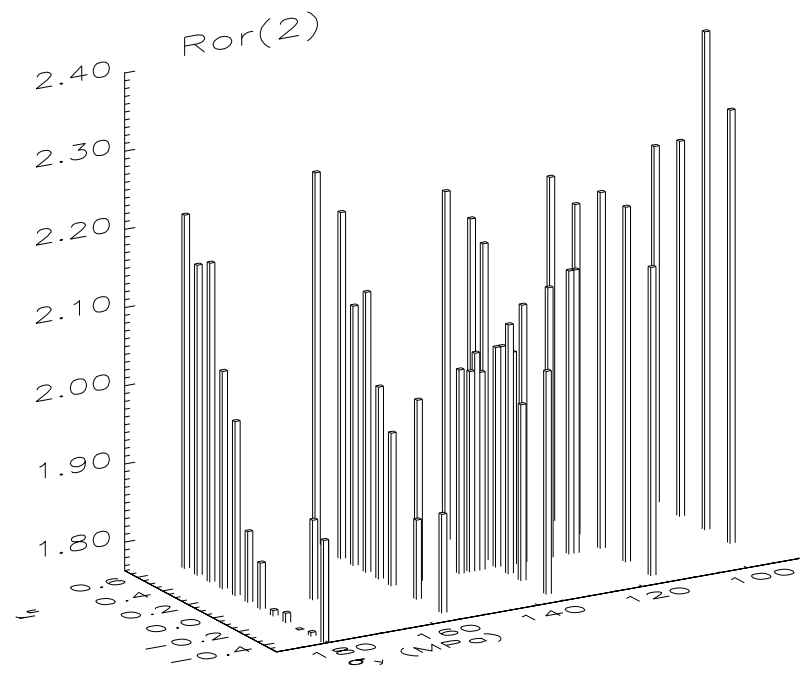

Fig. 12. $Ror(2)$ as a function of σ_y and r_n. The quantity $Ror(2)$ is the temporal average of the reciprocal Urey number over the last 2000 Ma. Further explanations see Figs. 10 and 11.
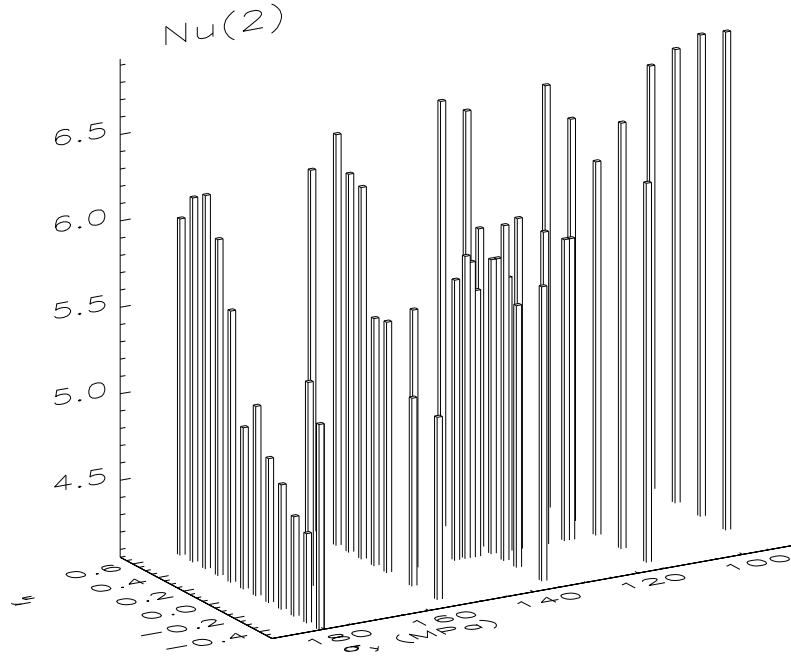
Fig. 13. $Nu(2)$ as a function of σ_y and r_n. The quantity $Nu(2)$ is the temporal average of the Nusselt number over the last 2000 Ma. Further explanations see Figs. 10 and 11.

3.3 Solutions using viscosity profiles of other authors

We have solved the system of differential equations of the mantle's evolution, (9) to (13), also for some totally different proposals regarding the viscosity distribution in the mantle: For each viscosity proposal, we did not use only one run but we covered the whole mentioned Ra_H–σ_y area over with runs. For lack of space, only the best solution of each set of runs is shown where the word best refers to the plateness near the surface connected with simultaneous thin sheet-like downwellings in the depth.

Kaufmann and Lambeck (2002) used a formal inverse procedure to derive radial viscosity profiles where they used mainly palaeo-shorelines, present-day sea level data and rotational data. Supposing their profiles, we obtained the best results with the numerical data describing the viscosity profile of their Figure 5(a) and called it *etaKL5a*. Profile *etaKL5a* has been derived from 569 relative sea level change data, the observed true polar wander velocity and the rate of change of the spherical harmonic degree-two component of the gravitational field. Using *etaKL5a*, we obtained the best run with $\sigma_y = 180\ MPa$ and $r_n = 1.5$. The upper panel of Fig.14 shows a quite possible present-day temperature profile, the lower panel stands for the corresponding present-day viscosity profile. The viscosity of the asthenosphere is unacceptable. However, if we use the directly given viscosity values, i.e., *etaKL5a* with $r_n = 0$, then no significant solution could be found. The temporal dependence of the laterally
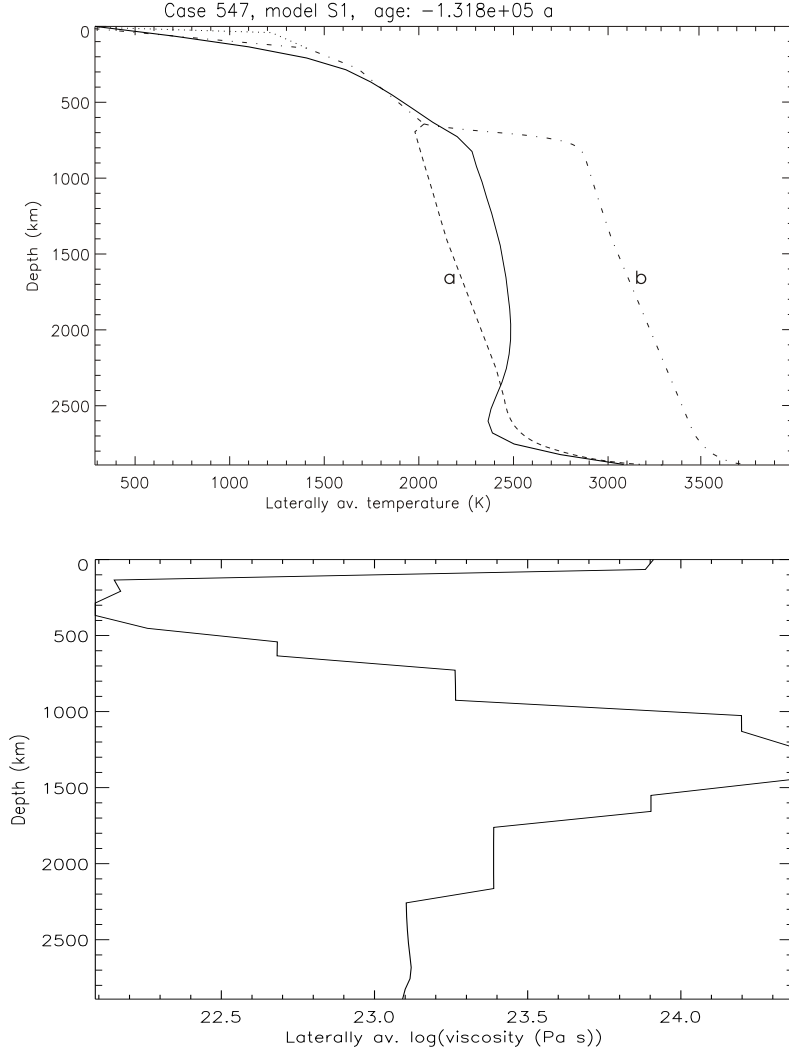
21

Fig. 14. Upper panel: The present-day laterally averaged temperature as a function of depth using the optimum evolution solution presupposed that *etaKL5a* (Kaufmann and Lambeck, 2002) is the right relative viscosity profile of the mantle. $\sigma_y = 180\,MPa$ and $r_n = 1.5$ apply for that optimum solution that is called case 547. Lower panel: The present-day laterally averaged viscosity as a function of depth for case 547.

averaged heat flow of the best evolution solution with *etaKL5a* is in the proper order of magnitude but somewhat smooth. As expected, the reciprocal Urey number, Ror, rises with decreasing age, τ, but is somewhat to low. $Ra_H(\tau)$ is acceptable, $EkinUM(\tau)$ is too smooth [see Fig.A.1]. Using our viscosity profile *eta3* (Fig.2), the velocity vectors (arrows) of each plate are distributed in the sense of a unified rotation around the center of the Earth not only at the surface but also e.g. in 134.8 km depth for a certain σ_y–$Ra_H(2)$ area (Fig.10) whereas Fig.15 with *etaKL5a* scarely shows such a behavior. However, Fig.15 displays thin blue subducting zones that can be seen also in 632.9 km depth at nearly the same place, yet, but with somewhat vague outlines [see Fig.A2]. We calculated another set of solutions using the viscosity profile

22

Case 547
Tcmb Var.3a KL5a* ys=1.8e8 Pa
Depth   =   1.348e+02 km
Time   =   4.490e+09 a   Age = −1.321e−01 Ma
Max vel =   1.379e+00 cm/a   Av hor vel =   4.633e−01 cm/a

Temperature
(K)

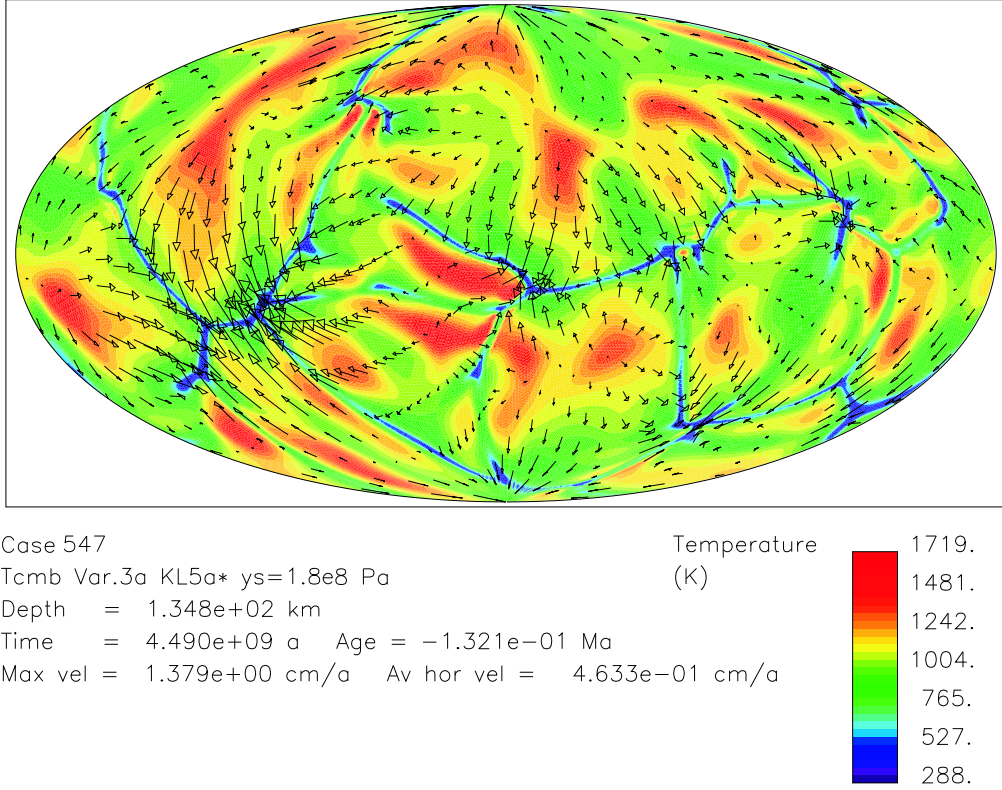| 1719. |
| 1481. |
| 1242. |
| 1004. |
| 765. |
| 527. |
| 288. |

Fig. 15. Equal-area projection of the temperature and creeping velocity distributions for the present day and 134.8 km depth of run 547 using the Kaufmann-Lambeck type of viscosity profile (See text and Fig.14)

by King and Masters (1992). In sharp contrast to *eta3*, that profile has a low-viscosity transition layer. King and Masters (1992) used an inverse procedure to infer their viscosity profile, called *etaKM*, from the shear-wave velocity distribution, the geoid, and an eleven-layer parameterization. We investigated the evolution solutions with *etaKM* again in the mentioned σ_y–$Ra_H(2)$ parameter range and present the best solution with *etaKM*. This solution is given by run 628 for $\sigma_y = 135\ MPa$ and $r_n = 0.5$. The upper panel of Fig.16 depicts the present-day temperature profile. It is by no means unrealistic. The lower panel shows the corresponding viscosity profile. Between 200 and 410 km depth, the viscosity is much too high. For $r_n = 0$ and *etaKM*, however, it was impossible to find a significant solution. The laterally averaged heat flow of run 628 has the right order of magnitude but it is somewhat too low. As expected, *Ror* rises as a function of time but the curve is somewhat too low. $Ra_H(\tau)$ is acceptable, $EkinUM(\tau)$ looks less reliable [See Fig.A3]. Fig 17 presents the best possible creeping velocity distribution and temperature for the geological present in 134.8 km depth, that is allowed by *etaKM*. There is a wide-meshed network of elongated downwellings, however, inside a cell, the creeping velocities are not plate-like near the surface. Since run 628 is the best one for the King-Masters profile, there are no plate-like solutions at all for other r_n and σ_y. Also other physical quantities show slight to strong
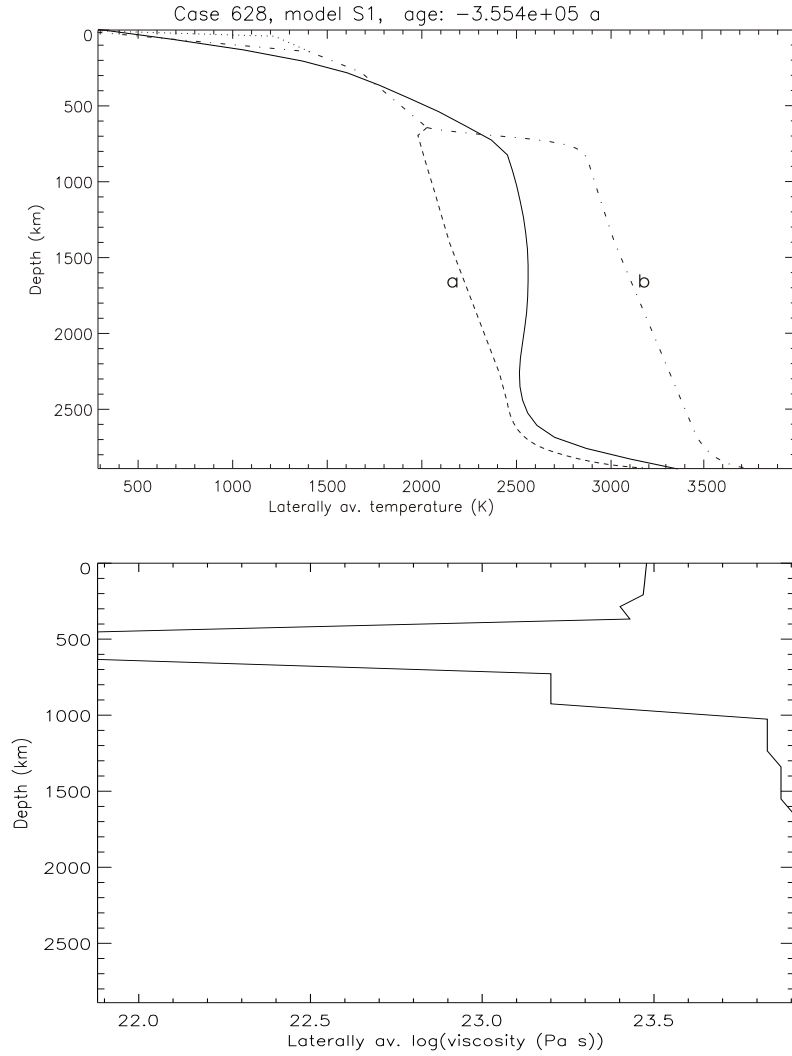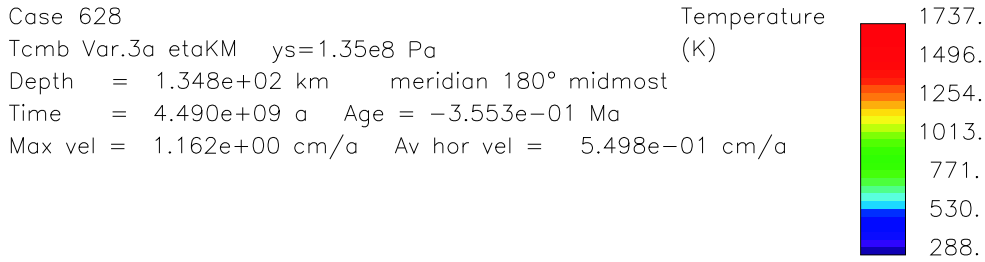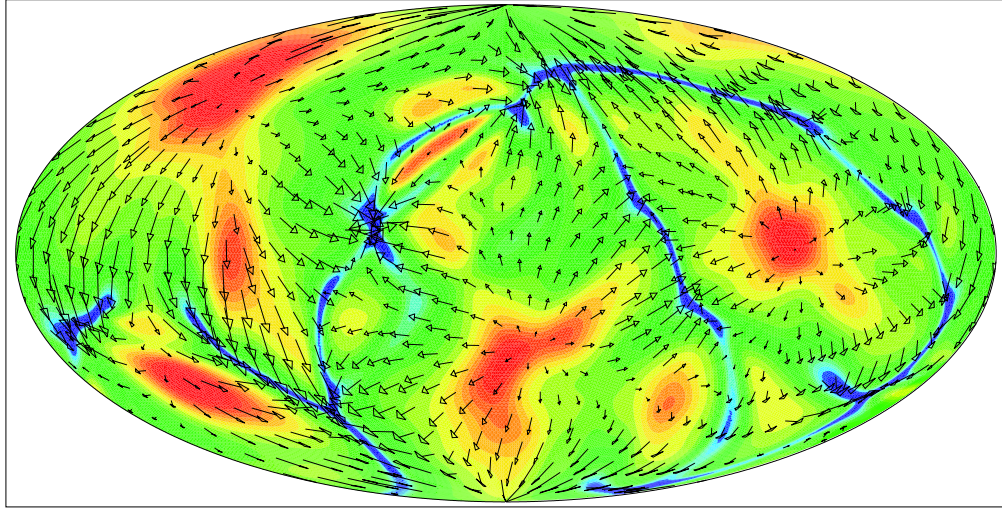
23

Fig. 16. Upper panel: The present-day laterally averaged temperature as a function of depth using the optimum evolution solution presupposed that *etaKM* (King and Masters, 1992) is the true relative viscosity profile of the mantle. $\sigma_y = 135\ MPa$ and $r_n = 0.5$ apply for that optimum solution that is called case 628. Lower panel: The present-day laterally averaged viscosity as a function of depth for case 628.

derivations from observational or expected values. However, the subducting downwellings of Fig.17 can be detected in 632.9 km depth, yet [See Fig.A.4]. A more geophysical discussion of these sets of runs and a comparison of the results for the very different viscosity profiles *eta3*, *etaKL5a* and *etaKM* can be found in Section 4. Very simple viscosity profiles, e.g. a constant mantle viscosity or a jump by factor of 30 at 660 km depth have not been investigated in this paper since already Bunge et al. (1997) studied these cases.

Case 628
Tcmb Var.3a etaKM   ys=1.35e8 Pa
Depth   = 1.348e+02 km   meridian 180° midmost
Time   = 4.490e+09 a   Age = −3.553e−01 Ma
Max vel = 1.162e+00 cm/a   Av hor vel =   5.498e−01 cm/a

Temperature
(K)

1737.
1496.
1254.
1013.
771.
530.
288.

Fig. 17. Equal-area projection of the temperature and creeping velocity distributions for the present day and 134.8 km depth of run 628 using the King-Masters type of viscosity profile (See text and Fig.16).

3.4 eta3-solutions using a not only laterally but also temporally constant CMB temperature

Some of the runs collected in Fig.10 have been repeated by averaging the originally only laterally constant CMB temperatures, T_c, over the time, taking this temporal mean of T_c as new thermal boundary condition at CMB and repeating the runs with laterally *and temporally* constant T_c. The resulting alterations of the character of the solution are not very impressive. The profile of the laterally averaged temperature is somewhat higher for all runs and all ages. The repetition of our reference run is run 599. The present-day temperature profile of run 599 is given by short dashes in Fig.3 to compare it with that of the reference run. The present-day laterally averaged viscosity of run 599 is very similar to Fig.4. The laterally averaged heat flows, Ror, Ra_H, and the kinetic energies of the upper mantle as a function of time are similar to those of the corresponding twin run but of course not in all details [See Fig.A.5]. Only the plateness is much less pronounced but present, yet [See Fig.A.6]. There are also thin downwelling sheets in 632.9 km depth, yet [See Fig.A.7].

25

4 Discussion and conclusions

Each conclusion begins with a lowercase letter. It is followed by a short discussion.

a) Based on geophysically observable quantities, the *Grüneisen parameter*, the specific heat at constant pressure, the specific heat at constant volume and the *melting temperature*, T_m, have been computed *as functions of radius* using well-known physical formulae. - We presented only $T_m(r)$ for sake of brevity. Based on the assumption that the eutectic composition of the lower mantle is nearly perovskitic and using the homologous temperature, T/T_m, already van Keken and Yuen (1995) concluded that the viscosity strongly increases with depth in the lower mantle. We introduced our approach in Section 2.1. to become less dependent on geochemical and mineralogical assumptions. Boehler (2000) summarized some important experimental upper bounds for T_m of the probably prevailing minerals of the lower mantle. Fig.1 shows that our $T_m(r)$ curve is well compatible with other geophysical findings.

b) We derived a *new mantle viscosity profile, eta3*. New features of this profile are a *high-viscosity transition layer* beneath the usual asthenosphere, *a second low-viscosity layer* in the uppermost part of the lower mantle and a *strong viscosity increase* in the central region of the lower mantle. It is mainly a consequence of the temperature dependence of the viscosity that generates the top and bottom thermal boundary layers of the mantle. These layers are already a part of the derived profile: A highly viscous oceanic lithosphere is at the top, a low-viscosity boundary layer is on CMB. No continental chemical boundary layer is included in the model, yet. The other variations of the profile are induced mainly by the pressure. The strong viscosity decrease as a function of depth under the transition layer is in a layer of 50-100 km thickness. It is probably somehow connected with the dissociation of garnets to perovskites and Al_2O_3 (Cf. Section 2.1.3.). - It follows a short discussion on results of other authors that gave already hints to conclusion b): Čížková et al. (1996) and Kido and Čadek (1997) also argued for the existence of a high viscosity transition layer and of two low viscosity layers, one above and one below of it. They started from a distribution of the seismic velocities by Li and Romanowicz (1996), transformed the seismic velocities into densities, and used a genetic algorithmic inversion that excluded those parts of the mantle where the density differences have predominantly compositional causes. Using intermediate-wavelength geoid inversions, Kido and Yuen (2000) studied the viscosity profile of the mid-mantle in detail. They found it to be of no major consequence whether they introduced an impermeable boundary at 660, 700, 750, or even 1000 km depth or whether there was no impermeable boundary. In all cases they obtained similar viscosity profiles, namely, a high viscosity lithosphere, followed by a low viscosity asthenosphere, followed by a high-viscosity transition layer, followed by a second low viscosity layer in the uppermost part

of the lower mantle. Their curves are similar to the upper half of Fig.2. They did not show the profile for the lower half of the mantle because of low resolution. Forte (2000) derived a set of viscosity profiles through a formal inversion procedure. His profiles produce a best fit to the observed free-air anomalies and to the observed motions of the lithospheric plates where his starting point was a pair of seismic tomography models. When an impermeable boundary is assumed at 670 km depth, the resulting viscosity-depth curve is similar to our Fig.2. Without this impermeable boundary, the viscosity peak, corresponding to the transition layer, is shifted down by 240 km. Furthermore, it is remarkable that *eta3* bears a certain similarity to the successful viscosity profile LVZ of Cserepes et al. (2000, p.139). We note that the mentioned profiles have been derived in a totally different way than Fig.2.

c) We introduced a viscoplastic yield stress and obtained *plate-like movements* near the surface. Apart from that, the present model is Newtonian. The mentioned kind of plate generation is not new, but is was important for the heat balance of the system to introduce the yield stress since only a small part of the temperature dependence of the viscosity could explicitely be used for numerical reasons. However, the greater part of this dependence is indirectly included already in *eta3*, especially in the thermal boundary layers. - Already Tackley (2000a) investigated the influence of viscoplastic yield stress where a part of it depended on depth. Tackley (2000b) studied the effect of increasing strain weakening. Richards et al. (2001) found that the generation of plates is facilitated by plastic yield stress and a low-viscosity asthenosphere beneath the lithosphere. Bercovici et al. (2001b,c,2002) and Ricard et al. (2001) examined a two-phase mixture to achieve a continuum description of weakening and shear localization and to explain the plate boundary formation. Continuing the work of Trompert and Hansen (1998), the Hansen group is working on the problem of the formation of oceanic lithosphere and subduction slabs, too. Nevertheless, it is evident that we solved the subduction problem only in a rough way, as far as it is necessary for a global mechanism. Because of the big grid size of present-day global models, it is not possible to include smaller regional or local effects as, e.g., small-scale convection under the back arc (Honda et al., 2002) or the detailed retreating mechanism of a slab (Funiciello et al., 2003). A further important issue would be the dehydration of harzburgite of the slab that occurs during partial melting. So, the slab viscosity will probably increase by 2-3 orders of magnitude (Mackwell et al., 1985; Karato et al., 1986; Mackwell and Kohlstedt, 1990; Hirth and Kohlstedt, 1996; Braun et al., 2000).

d) The results of our 3-D dynamical-evolution runs using *eta3* have been compared with sets of runs using rather *different viscosity profiles* with only one interior low-viscosity layer in different depths, namely *etaKL5a* (Kaufmann and Lambeck, 2002) and *etaKM* (King and Masters, 1992). This comparison reveals that *eta3 facilitates the generation of stable, plate-tectonic behavior near the surface and simultaneously thin sheet-like downwellings in the depth considerably more than etaKL5a or even etaKM.* It is evidently the existence

of *two internal low-viscosity layers* that causes this phenomenon. - Already Richards et al. (2001) found that one low-viscosity layer facilitates plate generation more than models without any asthenosphere.

e) 3-D dynamical-evolution runs with *eta3* but *without any yield stress* show *networks* of reticulary connected very thin cold sheet-like downwellings but, of course, no plates. Unfortunately, we cannot show the pictures here for lack of space. In the corresponding model calculations with *eta3 plus yield stress* of the usual order of magnitude, plate-like downwelling sheets continue to exist but their number is reduced. Some of them are loosely connected, other perpendicular sheets are isolated. So, *the distribution of the downwellings is more Earth-like if the yield stress is additionally used* (Cf. Figs. 6 to 9).

f) For a further quantification of the results, a systematic *variation of the parameters* was carried out for each basic viscosity profile. We varied a Rayleigh number, $Ra_H(2)$, and the yield stress, σ_y. But only for *eta3*, σ_y–$Ra_H(2)$ areas were found that clearly show a simultaneous occurrence of reproducible stable plate-like behavior near the surface *and* thin tabular-shaped downwellings.

g) In certain σ_y–$Ra_H(2)$ areas, all three basic viscosity profiles produce acceptable distributions of laterally averaged temperature as a function of depth. For $Ror(\tau)$, $EkinUM(\tau)$, etc, the results of runs with *eta3* are more realistic.

Acknowledgements

References

[1] Anonymous, 2004. Private communication.

[2] Balachandar, S., Yuen, D.A., Reuteler, D., 1992. Time dependent three-dimensional compressible convection with depth-dependent properties. Geophys. Res. Lett. 19, 2247-2250.

[3] Baumgardner, J.R., 1983. A three-dimensional finite element model for mantle convection. Thesis, Univ. of California, Los Angeles.

[4] Baumgardner, J.R., 1985. Three-dimensional treatment of convective flow in the Earth's mantle. J. Stat. Phys. 39 (5-6), 501-511.

[5] Bercovici, D., 1998. Generation of plate tectonics from lithosphere-mantle flow and void-volatile self-lubrication. Earth Planet. Sci. Lett. 154, 139-151.

[6] Bercovici, D., Ricard, Y., Schubert, G., 2001a. A two-phase model for compaction and damage. 1. General theory. J. Geophys. Res. 106, 8887-8906.

[7] Bercovici, D., Ricard, Y., Schubert, G., 2001b. A two-phase model for compaction and damage. 3. Application to shear localization and plate boundary formation. J. Geophys. Res. 106, 8925-8939.

[8] Bercovici, D., Ricard, Y. 2003. Energetics of a two-phase model of lithospheric damage, shear localization and plate-boundary formation, Geophys. J. Int., 152, 581-596.

[9] Boehler, R., 2000. High-pressure experiments and the phase diagram of lower mantle and core materials. Rev. Geophysics 38, 221-245.

[10] Braun, M.G., Hirth, G., Parmentier, E.M., 2000. The effects of deep damp melting on mantle flow and melt generation beneath mid-ocean ridges. Earth Planet. Sci. Lett, 176 (3-4), 339-356.

[11] Buffet, B.A., 2002. Estimates of heat flow in the deep mantle based on the power requirements for the geodynamo. Geophys. Res. Lett. 29, No. 12, 10.1029/2001 GL 014649, 7-1 .. 7-4.

[12] Bunge, H.P., Richards, M.A., 1996. The origin of large-scale structure in mantle convection. Effects of plate motions and viscosity stratification. Geophys. Res. Lett. 23, 2987-2990.

[13] Bunge, H.P., Richards, M.A., Baumgardner, J.R., 1996. Effect of depth-dependent viscosity on the planform of mantle convection. Nature 379,436-438.

[14] Bunge, H.-P., Richards, M.A., Baumgardner, J.R., 1997. A sensitivity study of three-dimensional spherical mantle convection at 10^8 Rayleigh number: effects of depth-dependent viscosity, heating mode, and an endothermic phase change. J. Geophys. Res. 102, 11991-12007.

[15] Christensen, U.R., 1984a. Convection with pressure-dependent and temperature-dependent non-Newtonian rheology. Geophys. J.R. Astron. Soc. 77, 343-384.

[16] Christensen, U.R., 1984b. Heat transport by variable viscosity convection and implications for the Earth's thermal evolution. Phys. Earth Planet. Inter. 35, 264-282.

[17] Christensen, U.R., Yuen, D.A., 1985. Layered convection induced by phase transitions. J. Geophys. Res 90, 10291-10300.

[18] Čížková, H., Čadek, O., Yuen, D.A., Zhou, H., 1996. Geoid slope spectrum and constraints on mantle viscosity stratification. Geophys. Res. Lett. 23, 3063-3066.

[19] Cserepes, L., 1993 Effect of depth-dependent viscosity on the pattern of mantle convection. Geophys. Res. Lett. 20, 2091-2094.

[20] Cserepes, L., Yuen, D. A., 1997. Dynamical consequences of mid-mantle viscosity stratification on mantle flows with an endothermic phase transition. Geophys. Res. Lett. 24,181-184.

[21] Cserepes, L., Yuen, D. A., Schroeder, B.A., 2000. Effect of the mid-mantle viscosity and phase-transition structure on 3-D mantle convection. Phys. Earth Planet. Inter. 118,135-148.

[22] Dubuffet, F., Yuen, D.A., Rabinowicz, M. 1999. Effects of a realistic mantle thermal conductivity on the patterns of 3-D convection. Earth Planet. Sci. Lett. 171, 401-409.

[23] Dumoulin, C., Doin, M.-P., Fleitout, L., 1999. Heat transport in stagnant lid convection with temperature- and pressure-dependent Newtonian or non-Newtonian viscosity, J. Geophys. Res. 104, 12759-12778.

[24] Dziewonski, A.M., Anderson, D.L., 1981. Preliminary reference Earth model. Phys. Earth Planet. Inter. 25, 297-356.

[25] Forte, A.M., 2000. Seismic-geodynamic constraints of mantle flow: implications for layered convection, mantle viscosity, and seismic anisotropy in the deep mantle. In: Karato, S.-I., Forte, A.M., Liebermann, R.C., Masters, G., Stixrude, L. (Eds.), Earth's Deep Interior. American Geophys. Union, Washington, DC, pp.3-36.

[26] Funiciello,F., Morra, G., Regenauer-Lieb, K., Giardini, D., 2003. Dynamics of retreating slabs: 1. Insights from two-dimensional numerical experiments. J. Geophys. Res. 108, no. B4, 2206, doi: 10.1029/2001JB000898

[27] Garnero, E.J., Helmberger, D.V., 1996. Seismic detection of a thin laterally varying boundary layer at the base of the mantle beneath the central Pacific. Geophys. Res. Lett. 23, 977-980.

[28] Gilvarry, J.J. 1956. The Lindemann and Grüneisen laws. Phys. Rev. 102, 307-316.

[29] Glatzmaier, G.A., 1988. Numerical simulations of mantle convection: Time-dependent, three-dimensional, compressible, spherical shell. Geophys. Astrophys. Fluid Dyn. 43, 223-264.

[30] Glatzmaier, G.A., Schubert, G., Bercovici, D., 1990. Chaotic, subduction-like downflows in a spherical model of convection in the Earth's mantle. Nature 347, 274-277.

[31] Gurnis, M., 1988. Large-scale mantle convection and the aggregation and dispersal of supercontinents. Nature, 332, 695-699.

[32] Gurnis, M., Davies, G.F., 1986. Numerical study of high Rayleigh number convection in a medium with depth-dependent viscosity. Geophys. J.R. Astron. Soc. 85, 523-541.

[33] Hansen, U., Yuen, D.A., Kroening, S.E., Larsen, T.B., 1993. Dynamic consequences of depth-dependent thermal expansivity and viscosity on mantle circulations and thermal structure. Phys. Earth Planet. Inter. 77, 205-223.

[34] Haskell, N.A., 1935. The motion of a fluid under a surface load 1. Physics 6, 265-269.

[35] Hirth, G., Kohlstedt, D.L., 1996. Water in the oceanic upper mantle: implications for rheology, melt extraction and the evolution of the lithosphere. Earth Planet. Sci. Lett. 144, 93-108.

[36] Hofmeister, A.M., 1999. Mantle values of thermal conductivity and the geotherm from phonon lifetimes. Science 283, 1699-1706.

[37] Holland, K.G., Ahrens, T.J., 1997. Melting of $(Mg,Fe)_2SiO_4$ at the core-mantle boundary of the Earth, Science 275, 1623-1625.

[38] Honda, S., Iwase, Y., 1996. Comparison of the dynamic and parameterized models of mantle convection including core cooling. Earth Planet. Sci. Lett. 139, 133-145.

[39] Honda, S., Saito, M., Nakakuki, T.; 2002. Possible existence of small-scale convection under the back arc. Geophys. Res. Lett. 29, no.21, 2043, doi: 10.1029/2002GL015853

[40] Honda, S., Yuen, D. A., 1994. Model for convective cooling of mantle with phase changes - Effects of aspect ratios and initial conditions. J. Phys. Earth 42, 165-186.

[41] Horai, K., Simmons, G., 1970. An empirical relationship between thermal conductivity and Debye temperature for silicates. J. Geophys. Res. 75, 978-982.

[42] Irifune, T., Ringwood, A.E., 1987. Phase transformations in primitive MORB and pyrolite compositions to 25 GPa and some geophysical implications. In: Manghnani, M.H., Syono, Y.(Eds.), High-Pressure Research in Mineral Physics, pp. 231-242, Geophysical Monograph 39, AGU, Washington, DC.

[43] Ito, E., 1989. Stability relations of silicate perovskite under subsolidus conditions. In: Navrotsky, A., Weidner, D.(Eds.), Perovskite: A Structure of Great Interest to Geophysics and Materials Science, pp. 27-32, Geophysical Monograph 45, AGU, Washington, DC.

[44] Ito,E., Takahashi, E., 1987. Melting of peridotite at uppermost lower-mantle conditions. Nature 328, 514-517.

[45] Karato, S.-i., 1997. Phase transformations and rheological properties of mantle minerals. In: Earth's Deep Interior, pp. 223-272, ed. Crossley, D.J., Gordon & Breach Sci. Publ., Amsterdam.

[46] Karato, S.-i., Li, P., 1992. Diffusion creep in perovskite: implications for the rheology of the lower mantle. Science 255, 1238-1240.

[47] Karato, S.-i., Paterson, M.S., Fitzgerald, J.D., 1986. Rheology of synthetic olivine aggregates: influence of grain size and water. J. Geophys. Res. 91, 8151-8176.

[48] Karato, S.-i., Riedel, M.R., Yuen, D.A., 2001. Rheological structure and deformation of subducted slabs in the mantle transition zone: implications for mantle circulation and deep earthquakes. Phys. Earth Planet. Inter. 127, 83-108.

[49] Karato, S.-i., Wang, Z., Liu, B., Fujino, K., 1995, Plastic deformation of garnets: systematics and implications for the rheology of the mantle transition zone. Earth Planet. Sci. Lett. 130, 13-30.

[50] Karato, S.-i. Wu, P., 1993. Rheology of the upper mantle: a synthesis. Science 260, 771-778.

[51] Kaufmann, G., Lambeck, K., 2002. Glacial isostatic adjustment and the radial viscosity profile from inverse modeling. J. Geophys. Res. 107, no. B11, 2280,doi: 10.1029/2001JB000941.

[52] Kido, M., Čadek, O., 1997. Inferences of viscosity from the oceanic geoid: Indication of a low viscosity zone below the 660-km discontinuity. Earth Planet. Sci. Lett., 151, 125-137.

[53] Kido, M., Yuen, D.A., 2000. The role played by a low viscosity zone under a 660-km discontinuity in regional mantle layering. Earth Planet. Sci. Lett. 181, 573-583.

[54] King, S.D., Masters, G., 1992. An inversion for radial viscosity structure using seismic tomography. Geophys. Res. Lett. 19, 1551-1554.

[55] Kirby, S.H., Stein, S., Okal, E.A., Rubie,D.C., 1996. Metastable mantle phase transformations and deep earthquakes in subducting oceanic lithosphere. Rev. Geophys. 34, 261-306.

[56] Li, P., Karato, S.-i., Wang, Z., 1996. High-temperature creep in fine-grained polycristalline $CaTiO_3$, an analogue material of $(Mg,Fe)SiO_3$ perovskite. Phys. Earth Planet. Inter. 95, 19-36.

[57] Li, X.D., Romanowicz, B., 1996. Global mantle shear velocity model developed using nonlinear asymptotic coupling theory. J. Geophys. Res. 101, 22245-22272.

[58] Lindemann, F.A., 1910. Über die Berechnung molekularer Eigenfrequenzen. Phys. Z. 11, 609-612.

[59] Lowman, J.P., Jarvis, G.T., 1999. Effects of mantle heat source distribution on supercontinent stability. J. Geophys. Res. 104, no. B6, 12733-12746.

[60] Mackwell, S.J., Kohlstedt, D.L., 1990. Diffusion of hydrogen in olivine: implications for water in the mantle. J. Geophys. Res. 95, 5079-5088.

[61] Mackwell, S.J., Kohlstedt, D.L., Paterson, M.S., 1985. The role of water in the deformation of olivine single crystals. J. Geophys. Res. 90, 11319-11333.

[62] Manga, M., Jeanloz, R., 1996. Implications of a metal-bearing chemical boundary layer in D" for mantle dynamics. Geophys. Res. Lett. 23, 3091-3094.

[63] McCulloch, M.T., Bennett, V.C., 1994. Progressive growth of the Earth's continental crust and depleted mantle: geochemical constraints. Geochim. Cosmochim. Acta 58, 4717-4738.

[64] Mitrovica, J.X., 1996. Haskell[1935] revisited. J. Geophys. Res. 101, no. B1, 555-569.

[65] Monnereau, M., Quéré, S., 2001. Spherical shell models of mantle convection with tectonic plates. Earth Planet. Sci Lett. 184, 575-587.

[66] Narasimhan, M.N.L., 1993. Principles of Continuum Mechanics. Wiley, New York etc, 567 pp.

[67] Osako, M., Ito, E., 1991. Thermal diffusivity of $MgSiO_3$ perovskite. Geophys. res. Lett. 18, 239-242.

[68] Poirier, J.P., 1986. Dislocation mediated melting of iron and temperature of the Earth's core. Geophys. J. R. Astron. Soc. 85, 315-328.

[69] Pollack, H.N., Hurter, S.J., Johnson, J.R., 1993. Heat flow from the Earth's interior: analysis of the global data set. Rev. Geophys. 31, 267-280.

[70] Ranalli, G., 1998. Inferences on mantle rheology from creep laws. GeoResearch Forum 3-4, 323-340.

[71] Ricard, Y., Bercovici, D., Schubert, G., 2001. A two-phase model for compaction and damage. 2. Applications to compaction, deformation and the role of interfacial surface tension. J. Geophys. Res. 106, 8907-8924.

[72] Richards, M.A., Yang, W.-S., Baumgardner, J.R., Bunge, H.-P., 2001. Role of a low-viscosity zone in stabilizing plate tectonics: Implications for comparative terrestrial planetology. Geochem. Geophys. Geosystems 2 (paper no.2000GC000115) U1-U16.

[73] Richter, F.M., 1973. Finite amplitude convection through a phase boundary. Geophys. J.R. Astron. Soc. 35, 265-276.

[74] Ringwood, A.E., 1990.. Slab-mantle interactions: petrogenesis of intraplate magmas and structure of the upper mantle. Chem. Geol. 82, 187-207.

[75] Schatz, J.F., Simmons, G. 1972. Thermal conductivity of Earth materials at high temperatures. J. Geophys. Res. 77, 6966-6983.

[76] Schubert, G., Turcotte, D.L., Olson, P., 2001. Mantle Convection in the Earth and Planets. Cambridge Univ. Press, Cambridge, etc., 940 pp.

[77] Solomatov, V.S., 1995. Scaling of temperature-dependent and stress-dependent viscosity convection. Phys Fluids 7, 266-274.

[78] Solomatov, V.S., El-Khozondar, R., Tikare, V., 2002. Grain size in the lower mantle: constraints from numerical modeling of grain growth in two-phase systems. Phys. Earth. Planet. Inter. 129, 265-282.

[79] Stacey, F.D., 1992. Physics of the Earth, 3rd ed., Brookfield Press, Brisbane, 513 pp.

[80] Stacey, F.D., 1996. Thermoelasticity of $(Mg,Fe)SiO_3$ perovskite and a comparison with the lower mantle. Phys. Earth Planet. Inter. 98, 65-77.

[81] Stacey, F.D., Stacey, C.H.B., 1999. Gravitational energy of core evolution: implications for thermal history and geodynamo power. Phys. Earth Planet. Inter. 110, 83-93.

[82] Steinbach, V., Yuen, D.A.,1997. Dynamical effects of a temperature-dependent and pressure-dependent lower-mantle rheology on the interaction of upwellings with the transition zone. Phys. Earth Planet. Inter. 103, 85-100.

[83] Steinbach, V., Yuen, D.A., 1994. Effects of depth-dependent properties on the thermal anomalies produced in flush instabilities from phase transitions. Phys. Earth Planet. Inter. 86, 165-183.

[84] Steinbach, V., Yuen, D.A., 1999. Viscous heating: a potential mechanism for the formation of ultralow velocity zone. Earth Planet. Sci. Lett. 172, 213-220.

[85] Steinbach, V., Yuen, D.A., Zhao, W.L., 1993. Instabilities from phase transitions and the timescales of mantle thermal evolution. Geophys. Res. Lett. 20, 1119 - 1122.

[86] Tackley, P.J., 1996. Effects of strongly variable viscosity on three-dimensional compressible convection in planetary mantles. Geophys. Res. Lett. 23, 1985-1988.

[87] Tackley, P.J., 1998. Self-consistent generation of tectonic plates in three-dimensional mantle convection. Earth Planet. Sci. Lett. 157, 9-22.

[88] Tackley, P.J., 2000a. Self-consistent generation of tectonic plates in time-dependent, three-dimensional mantle convection simulations. 1. Pseudoplastic yielding. Geochem. Geophys. Geosystems 1 (Paper no. 2000GC000043)

[89] Tackley, P.J., 2000b. Self-consistent generation of tectonic plates in time-dependent, three-dimensional mantle convection simulations. 2. Strain weakening and asthenosphere. Geochem. Geophys. Geosystems 1 (Paper no. 2000GC000044).

[90] Thompson, A.B., 1992. Water in the Earth's upper mantle. Nature 358, 295-302.

[91] Tozer, D.C., 1972. The present thermal state of the terrestrial planets. Phys. Earth Planet. Inter. 6, 182-197.

[92] van den Berg, A.P., Yuen, D.A., Allwardt, J.R., 2002. Non-linear effects from variable thermal conductivity and mantle internal heating: implications for massive melting and secular cooling of the mantle. Phys. Earth Planet. Inter. 129, 359-375.

[93] van Keken, P.E., Yuen, D.A., 1995. Dynamical influences of high viscosity in the lower mantle induced by the steep melting curve of perovskite: Effects of curvature and time dependence. J. Geophys. Res. 100, 15233-15248.

[94] Trompert, R.A., Hansen, U., 1998. Mantle convection simulations with rheologies that generate plate-like behavior. Nature 395, 686-689.

[95] Walzer. U., Hendel, R., 1999. A new convection-fractionation model for the evolution of the principal geochemical reservoirs of the Earth's mantle. Phys. Earth Planet. Inter. 112, 211-256.

[96] Walzer, U., Hendel, R., Baumgardner, J., 2003. Viscosity stratification and a 3-D compressible spherical shell model of mantle evolution. In: Krause, E., Jäger, W., Resch, M., (Eds.), High Performance Computing in Science and Engineering '03. Springer-Verlag, Berlin Heidelberg New York. pp. 27-67. ISBN 3-540-40850-9

[97] Walzer, U. Hendel, R., Baumgardner, J. Toward a thermochemical model of the evolution of the Earth's mantle. In: Krause, E., Jäger, W., Resch, M., (Eds.), High Performance Computing in Science and Engineering '04. Springer-Verlag, Berlin Heidelberg New York. 40pp. (submitted for publication).

[98] Weidner, D.J., Chen, J. Xu,Y., Wu, Y., Vaughan, M.T., Li, L., 2001. Subduction zone rheology. Phys. Earth Planet. Inter. 127, 67-81.

[99] Weinstein, S.A., 1998. The effect of convection planform on the toroidal-poloidal energy ratio. Earth Planet. Sci. Lett. 155, 87-95.

[100] Yamazaki, D., Kato, T., Ohtani, E., Toriumi, M., 1996. Grain growth rates of $MgSiO_3$-perovskite and periclase under lower mantle conditions. Science 274, 2052-2054.

[101] Yang, W.-S., 1997. Variable viscosity thermal convection at infinite Prandtl number in a thick spherical shell. Thesis, Univ. of Illinois, Urbana-Champaign.

[102] Yuen, D.A. , Balachandar, S., Steinbach, V.C. , Honda, S. , Reuteler, D.M., Smedsmo, J.J. , Lauer, G.S. , 1995. Non-equilibrium effects of core-cooling and time-dependent internal heating on mantle flush events. Nonlinear Processes in Geophysics, 2, 206-221.

[103] Zerr, A., Diegeler,A., Boehler, R., 1998. Solidus of the Earth's deep mantle. Science 281, 243-245.

[104] Zhang, J., Herzberg, C., 1994. Melting experiments on anhydrous peridotite KLB-1 from 5.0 to 22.5 GPa. J. Geophys. Res. 99, 17729-17742.
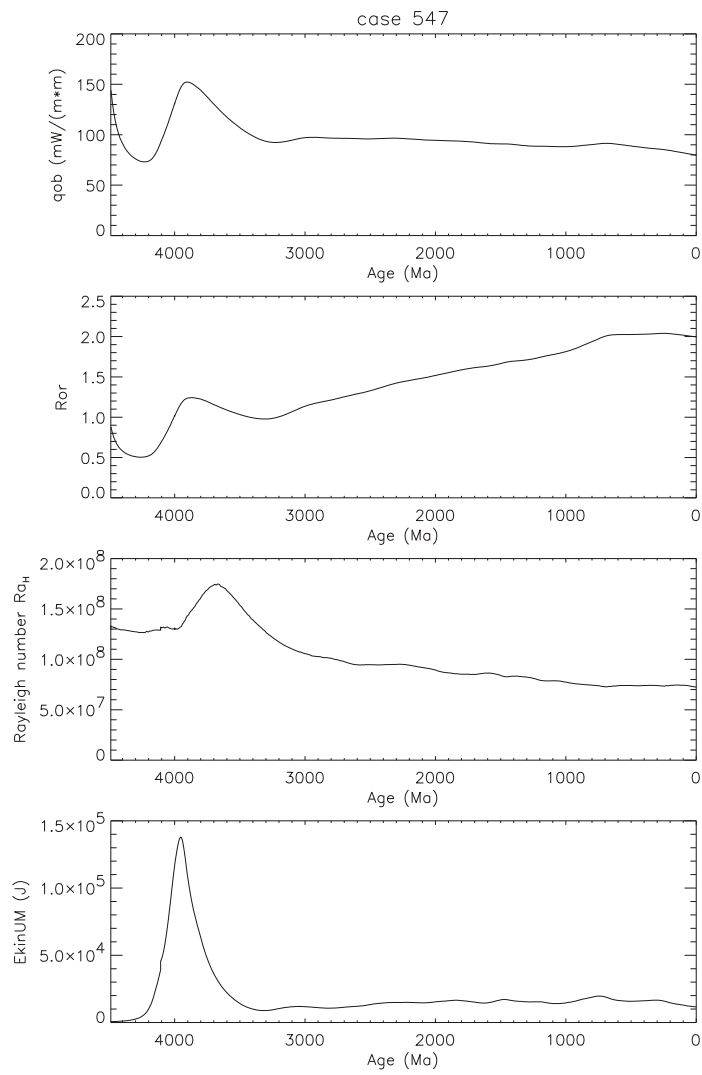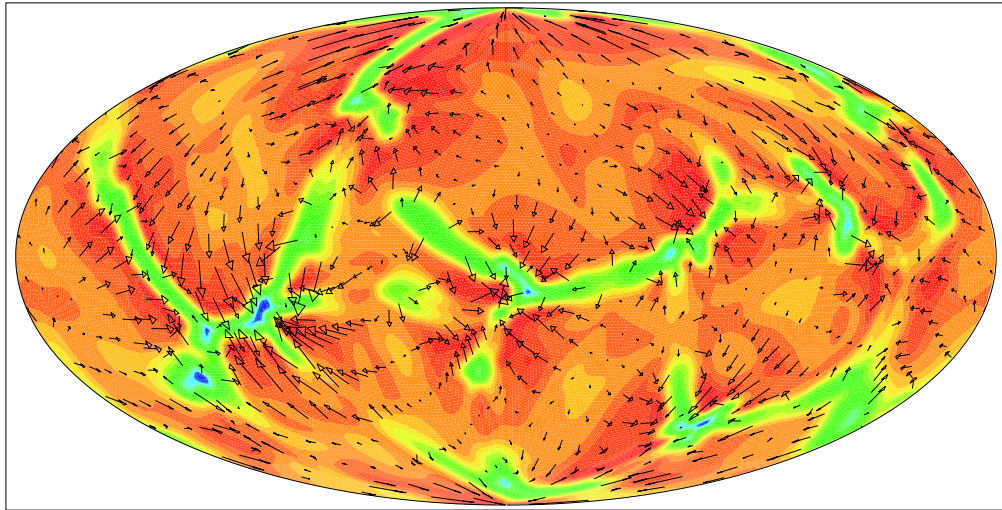
A   Appendix

Fig. A.1. The quantities *qob*, *Ror*, *Ra$_H$* and *EkinUM* as functions of age (See text and Fig. 5). These plots apply for *etaKL5a* and case 547 (See Fig. 14).

Case 547
Tcmb Var.3a KL5a* ys=1.8e8 Pa
Depth   =   6.329e+02 km
Time   =   4.490e+09 a   Age = −1.321e−01 Ma
Max vel =   1.091e+00 cm/a   Av hor vel =   1.391e−01 cm/a

Temperature
(K)

2855.
2428.
2000.
1572.
1144.
716.
288.

Fig. A.2. Equal-area projections of the temperature and creeping velocity distributions for the present day and 632.9 km depth. This applies for *etaKL5a* and case 547 (See Fig. 14).
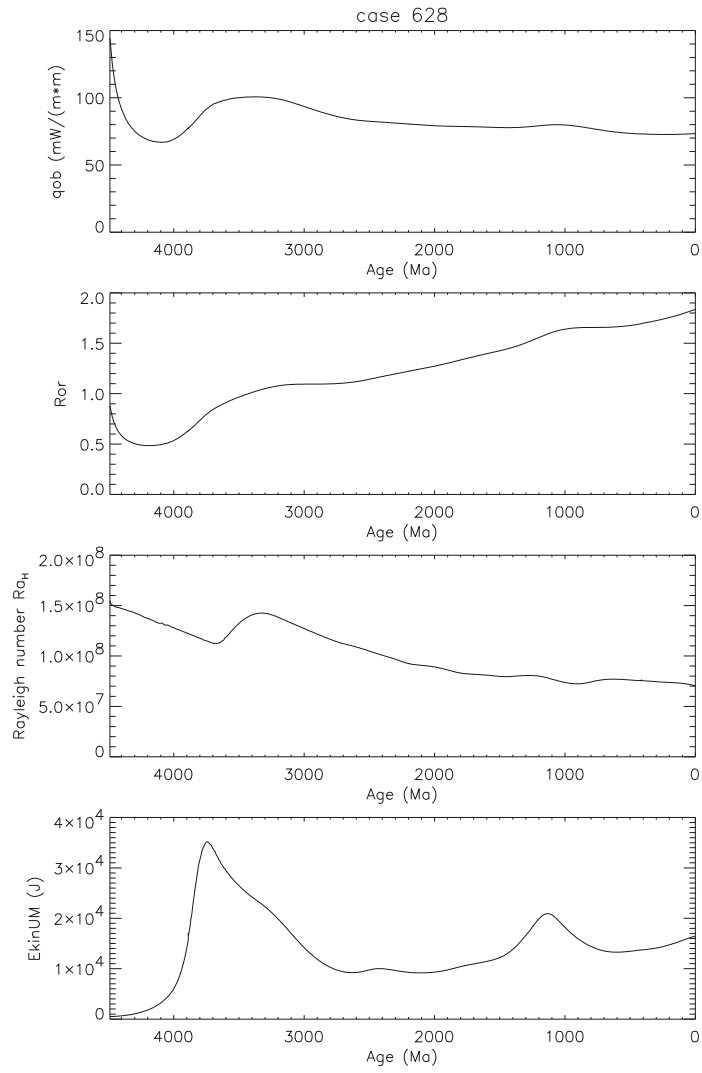
Fig. A.3. Supposing *etaKM* and case 628 (See Fig. 16), the following quantities as function of age are presented: *qob*, *Ror*, Ra_H, *EkinUM* (See text).
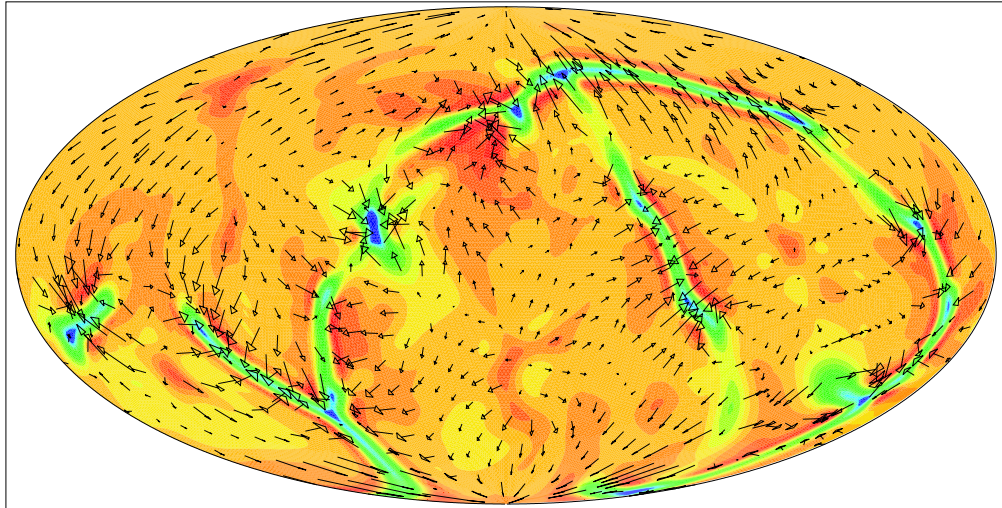
38

Case 628
Tcmb Var.3a etaKM   ys=1.35e8 Pa
Depth   =   6.329e+02 km   meridian 180° midmost
Time   =   4.490e+09 a   Age = −3.553e−01 Ma
Max vel =   1.703e+00 cm/a   Av hor vel =   1.383e−01 cm/a

Temperature
(K)

3219.
2731.
2242.
1754.
1265.
777.
288.

Fig. A.4. Supposing $etaKM$ and run 628 (See Fig. 16), the equal-area projection of the temperature and creeping velocity distributions for the present day and 623.9 km depth is shown.
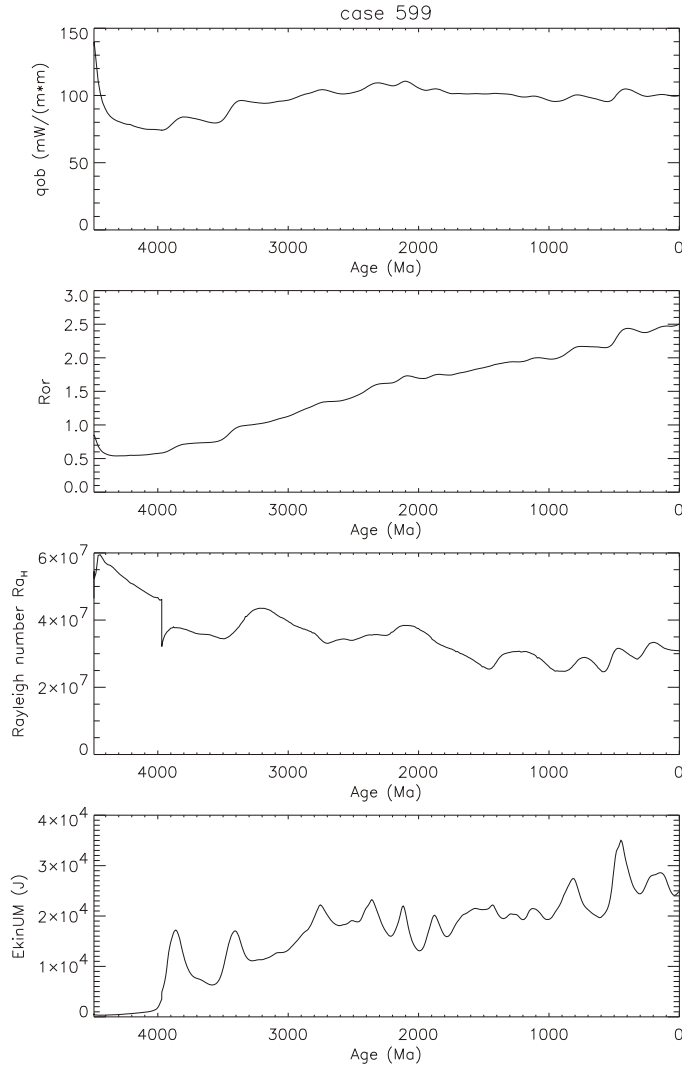
Fig. A.5. The quantities *qob*, *Ror*, *Ra$_H$* and *EkinUM* as a function of age for the viscosity profile *eta3* and, however, for a not only laterally but also *temporally* constant CMB temperature. All other data as in the reference run.
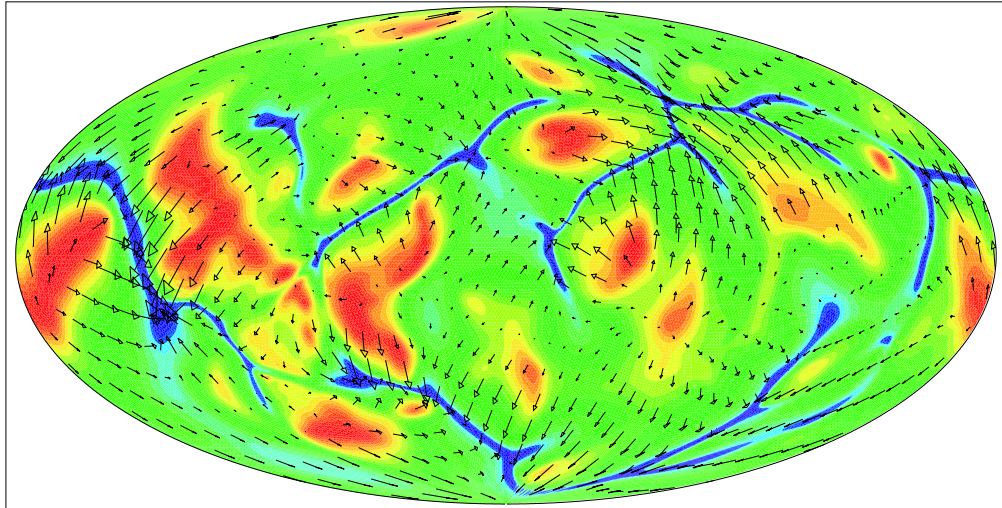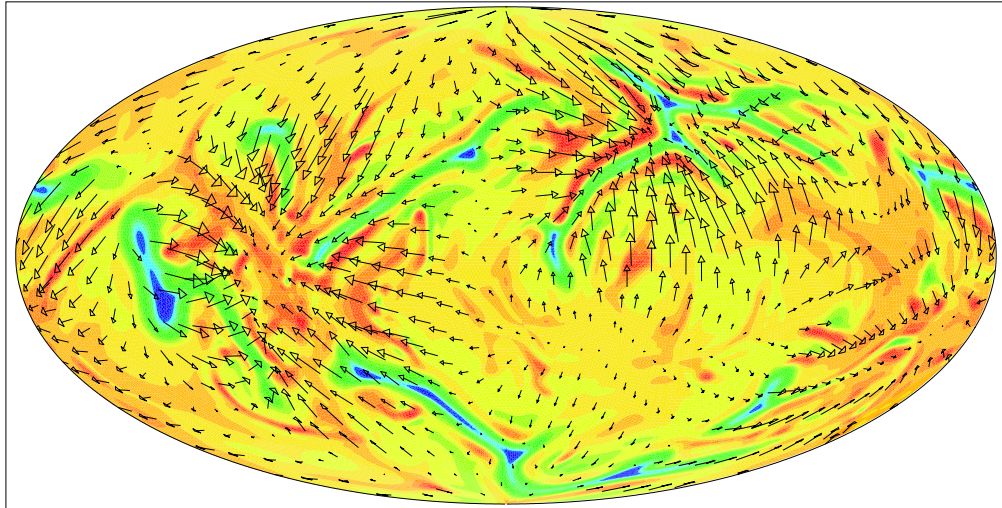
40

Case 599
eta3 ys=1.35e8 Pa
Depth   =   1.348e+02 km   meridian 180° midmost
Time   =   4.491e+09 a   Age = −9.180e−01 Ma
Max vel =   2.551e+00 cm/a   Av hor vel =   6.972e−01 cm/a

Temperature
(K)

2276.
1944.
1613.
1282.
951.
619.
288.

Fig. A.6. Equal-area projection of the temperature and creeping velocity distributions for the present day and 134.8 km depth for *eta*3 and for not only laterally but also temporally constant CMB temperature.

41

Case 599
eta3 ys=1.35e8 Pa
Depth   =   6.329e+02 km   meridian 180° midmost
Time   =   4.491e+09 a   Age = −9.180e−01 Ma
Max vel =   1.501e+00 cm/a   Av hor vel =   2.680e−01 cm/a

Temperature
(K)

3416.
2895.
2373.
1852.
1331.
809.
288.

Fig. A.7. Equal-area projection of the temperature and creeping velocity distributions for the present day and 632.9 km depth for *eta*3 and for not only laterally but also temporally constant CMB temperature.

B   Appendix

B.1. Model shortcomings. Discussion and future work.
There is no convection model of the Earth's mantle up to now that correctly reflects all known observational results. That is true for the present model, too. We will go through point by point and discuss the prospects for the further development of the model.

B.1.1. Convective vigor
The convective vigor of the present model is less than Earth-like, as indicated by surface velocities. The dimensional heat flux, however, is in the correct range. There is some unsureness regarding the thermal conductivity, k, and therefore also regarding the Nusselt number. Horai and Simmons (1970) and Schatz and Simmons (1972) concluded from a linear correlation between seismic P-wave velocity and thermal conductivity, that k grows from $3.3\frac{W}{mK}$ in the upper mantle to $20\frac{W}{mK}$ in the lower mantle. Glatzmaier et al. (1990) used $k = 23\frac{W}{mK}$ in their spherical-shell model. On the one hand the heat flow at CMB must be so that the model has the correct order of magnitude for the present-day inner core but on the other hand there must be enough energy to drive the geodynamo: Therefore, Stacey (1992) concluded a net CMB heat flow of $7.5TW$, assuming a temperature contrast of $1000K$ across a $200km$ thick D" boundary layer and a thermal lower-mantle conductivity of $10\frac{W}{mK}$. Osako and Ito (1991) measured a thermal conductivity of MgSiO$_3$-perovskite of $k = 5.1\frac{W}{mK}$. They predicted $k = 12\frac{W}{mK}$ for the lower part of the lower mantle (Cf. Schubert et al. 2001). Manga and Jeanloz (1997) modelled the pressure and temperature dependence of k of MgO and found $k = 5 - 12\frac{W}{mK}$ for the lower mantle. Therefore we assumed $k = 12\frac{W}{mK}$ for our model. In order to keep our different models comparable with each other, we did not change this value up to now although Hofmeister (1999) presented her new model. This semi-empirical model combined the phonon part and the photon part of thermal conductivity. Hofmeister's (1999) model leads to a k between 5.8 and $6.7\frac{W}{mK}$ at the top of the D" layer whereas $k = 3\frac{W}{mK}$ is the minimal value directly beneath the upper thermal boundary layer. Dubuffet et al. (1999) and van den Berg et al. (2002) studied the effects of Hofmeister's (1999) temperature- and pressure-dependent thermal conductivity on mantle convection. In these investigations, however, the viscosity is assumed to be *constant*, although the constant viscosity value has been varried from run to run in the paper by van den Berg et al. (2002). However, the present investigation is focussed on the effects of the pressure dependence of the viscosity. Buffet (2002) studied the heat flow in the deep mantle, too, where he took into account that the outer-core convection must supply energy to the geodynamo at a rate that compensates for the loss due to ohmic decay. He assumed $k = 10\frac{W}{mK}$ for the thermal conductivity of the mantle. Evidently, the question of the lower-mantle k still has to be clarified before a repetition of our many runs could make sense. Further-

more we expect that the effects of viscosity are more important for mantle convection than the influences of k .

B.1.2. Viscosity profiles, yielding and plate-like behavior
The usual approach to the problem of variable viscosity in mantle-convection models is to consider only the temperature dependence. So, the upper and the lower boundary of the mantle got a thermal boundary layer, each, with laterally varying thickness. In these other people's models, the mantle is virtually isoviscous between the two boundary layers. We showed above that an isoviscous interior of the mantle is impossible because of solid-state-physics and mineralogical reasons. Therefore we consider the isoviscous mantle interior of these other models to be an essential shortcoming since the influence of the viscosity is probably dominating in comparison to other physical parameters. Furthermore, it is evident that Newtonian viscosity cannot generate lithospheric plates at the surface if there are no additional assumptions regarding the constitutive equations. Therefore some other authors postulated rather complex constitutive equations. The setup of the present study is indeed very different from previous studies in that we firstly derive a viscosity profile as a function of the hydrostatic pressure and of the present-day temperature profile. In this derivation we used the realistic value of 17 for the quantity of c_t in the viscosity law, Eq.7. If we found a strong decrease of viscosity immediately above the CMB that is induced by a strong temperature rise in D" then this decrease is caused by the PREM temperature rise. In the self-consistent calculations we were able to use only $c_t = 1$ because of numerical limitations. Therefore, the lateral variation of the thickness of this boundary layer is only weak. Correspondingly, the lateral thickness variation of the lithosphere is weak, too. But this is the unaviodable price for the computational allowing for the large viscosity variations as a function of radius in the inertior of the mantle. So, a non-trivial future task is to improve the numerical procedure. The shortcoming of weak lateral thickness variations of the (up to now purely oceanic) lithosphere is reduced by the introduction of the yield stress, σ_y. The symmetry is broken by σ_y and by the small lateral variations due to $c_t = 1$. So, an Earth-like distribution of downwelling zones (Cf. Figs.6, 8 and 9) was formed showing *no* interconnected network. The introduction of σ_y into the model is largely simplified: Table B1 summarizes some well-known contrasts between Venus, Earth and Mars. The yield stress of the terrestrial lithosphere is evidently reduced in comparison with the lithosphere of Venus and Mars. Therefore, the latter planets don't have any present-day plate tectonics. In our preferred viscosity profile, the viscosity in the transition layer is high but somewhat less than that in the Earth's lithosphere. Since the transition layer has no direct contact to the ocean, the model assumed an infinite σ_y for those depths. Because of the existence of more than two phase transitions in the transition layer and because of the temperature dependence of the depth of the phase transitions, the grid-point density ought to be elevated in future for that zone.

Table B.1
Some essential differences between Venus, Earth and Mars

| Venus	Earth	Mars
a small quantity of water, but *no oceans*	a lot of water near the surface, polar caps of water ice, *oceans*	a small quantity of water near the surface, small polar caps of water ice, *no present-day oceans*
no life	life, therefore a thermostat at the surface	no life
composition of the atmosphere in volume percent		
96.5 % CO_2	0.03 % CO_2	95 % CO_2
3.5 % N_2	78 % N_2	2-3 % N_2
traces O_2	21 % O_2	0.1-0.4 % O_2
a hypsometric curve with only one peak	a hypsometric curve with two clearly divided culminations	a hypsometric curve with one main peak and some smaller maxima
no continents, small areas with granitoide rock	granitoide rocks in the upper continental crust	no continents
Gravity and topography are correlated.	Both geoid and gravity are not correlated with the distribution of continents and oceans.	Gravity and topography are correlated.
Volcanoes are stochastically distributed.	Volcanoes are distributed along a network of lines.	Younger volcanoes are are resticted to a small area, the Tharsis region.
Earthquake distribution is unknown up to now.	Big earthquakes are distributed along the same network lines.	Earthquake distribution is unknown up to now.
no plate tectonics	plate tectonics	no present-day plate tectonics
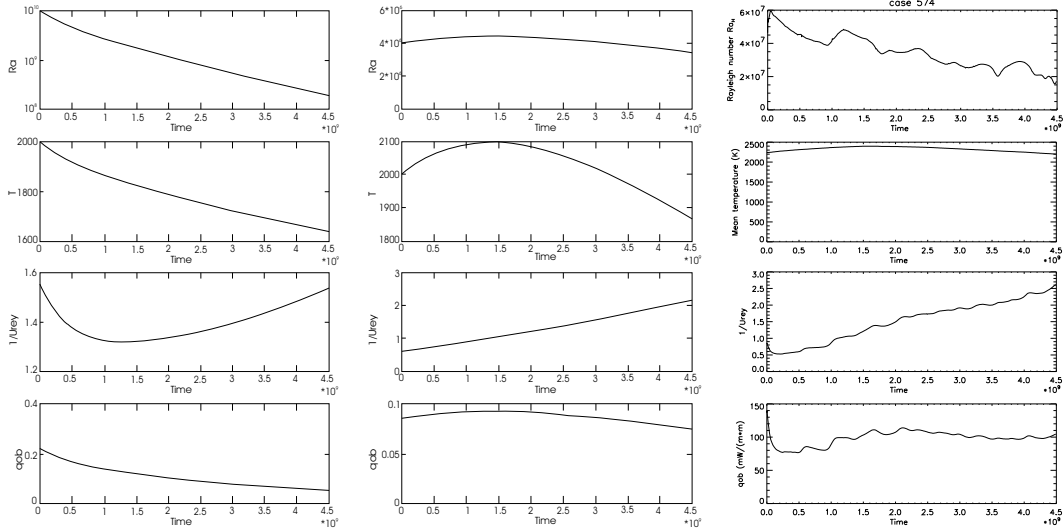
Fig. B.1. A comparison of the thermal evolution of some models. The first two columns have been provided by Anonymous (2004), the third column belongs to the present paper. On the left is a conventional parameterized model with the realistic viscosity-law constant $c_t = 17$, a thermal conductivity $k = 3\frac{W}{mK}$ that could be suitable for the upper mantle and with a high enough effective Rayleigh number, Ra, using the self-adjusting mechanism described by Tozer (1972). The central column presents a parameterized model with $c_t = 1$, $k = 12\frac{W}{mK}$ and an effective Rayleigh number set to match that of our case 574. On the right is our dynamical case 574.

B.1.3. Thermal evolution. A comparison

The essential innovations of this paper are the new viscosity profile, $\eta_3(r)$, of Fig.2 with two internal low-viscosity layers and very steep viscosity gradients as well as the generation of plateness near the surface and sheet-like downwellings with a realistic geometrical distribution of these downwellings in the spherical shell. Also other convection papers focus on certain particular aspects or investigate certain single mechanisms, mainly, but they have not been able to make all aspects Earth-like. Similarly, the long-term behavior of our system is not entirely realistic since we could use $c_t = 17$ only for the derivation of $\eta_3(r)$ but not in the dynamical model (Cf. Fig.B.1). For numerical reasons, we could not solve the system with Rayleigh numbers of 10^{10} at the beginning and 2×10^8 at the end of the evolution as it is possible for parameterized models. On the other hand, the parameterized model does not show temporal shorter-period variations although they could be relevant from the geological point of view. Because of the weak time dependence of the viscosity with $c_t = 1$ and because of the decaying heat production rate per unit volume, Q, the Rayleigh number, Ra_H, diminishes somewhat as a function of time (Cf. right column of Fig.B.1.). In the simplified parameterized model with $c_t = 1$, $k = 12\frac{W}{mK}$, Ra is nearly constant and decreases only slightly during the last 3 Ga. We conclude that the numerics of the code must be essentially improved to guarantee the solution of the system of equations for

46

higher Ra_H, $c_t = 17$, and for strong internal viscosity gradients. This is no short-range task. So, we present these intermediate results here. The mean temperatures, T_{mean}, as a function of time have been compared in the second line of Fig.B.1 for the three models presented there. In all three models, T_{mean} decreases by about 200K during the last 3Ga. This is realistic. At the beginning, however, our model shows a slight temperature rise. It is a consequence of our initial temperature. It is supposed to be 4000K at CMB and else adiabatic everywhere. The real initial temperatures could be essentially higher. Corresponding runs stopped working because of numerical difficulties. There could be a pertinent reason for the assumption of moderately high starting temperatures: The high abundances of Ni, Co, Cu, Re, Au, Ru, Rh, Os, Ir and Pt, occuring in approximately primordial C1 proportions, indicate that the upper mantle was never in thermodynamic equilibrium with the core. Fig.3 shows that our present-day temperature curve as a function of depth is situated well between geotherms of other dynamic models. [By the way, the steep temperature gradient between 300 and 800 km depth (Cf. Fig.3) is caused by high Grüneisen parameter values that have been derived from P, K and $\frac{dK}{dP}$ given by PREM using Eq.(5), and by the phase transitions. Of course, the upper mantle is convecting, too.] The present-day Urey number by Stacey and Stacey (1999) corresponds rather exactly with the corresponding value of the third column of Fig.B.1. The present-day value of the mean heat flow by Pollack et al. (1993) is virtually identical with the corresponding value, qob, of the third column of Fig.B.1. The temporal development of $\frac{1}{Urey}$ and qob would probably bring these curves nearer to the corresponding curves of the first column of Fig.B.1 if we would be able to execute the runs with $c_t = 17$.

B.1.4. Complement of the description of planforms
Fig.10 presents the distribution of the four types of solution in a $Ra_H(2) - \sigma_y$ plot. The Figs. 6, 8 and 9 are examples for the plate-like movement type that was depicted by little black disks with white center in Fig.10. Fig.B.2 represents the white-circle type of Fig.10. It shows a wide-meshed network of broad downwellings and has no plates at the surface. Fig.B.3 portrays the plus-type of Fig.10 and shows a diffuse disintegration of the network of cold areas near the surface. However, in 633 km depth and above there are single cold lines, yet, which correspond to subduction zones. But at the surface, there is no plate-like horizontal movement. Finally, the asterisk type of Fig.10 corresponds to a similarly disintegrated structure near the surface without plates, similar to Fig.B.3. But in the depth, the slab-like features dissapeared or showed some small remainders, at best (See e.g. Fig.B.4).
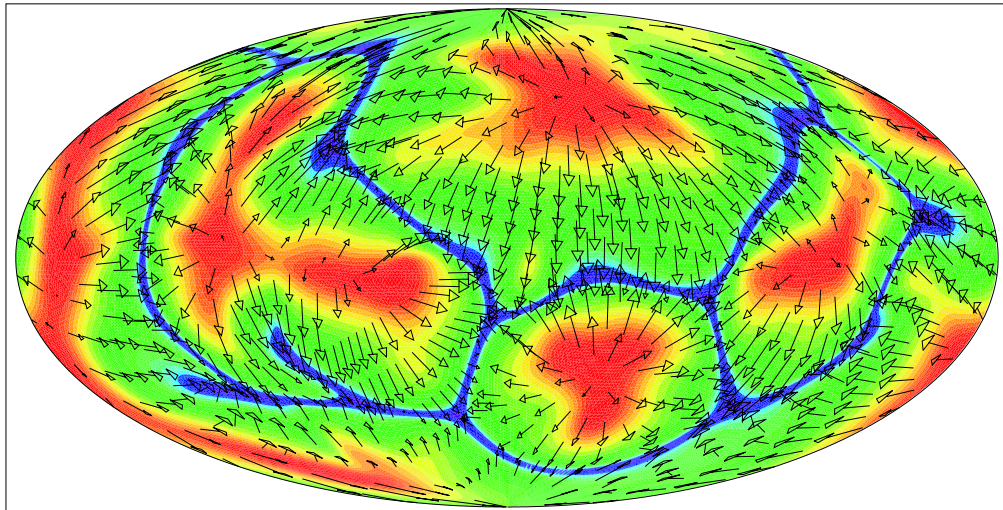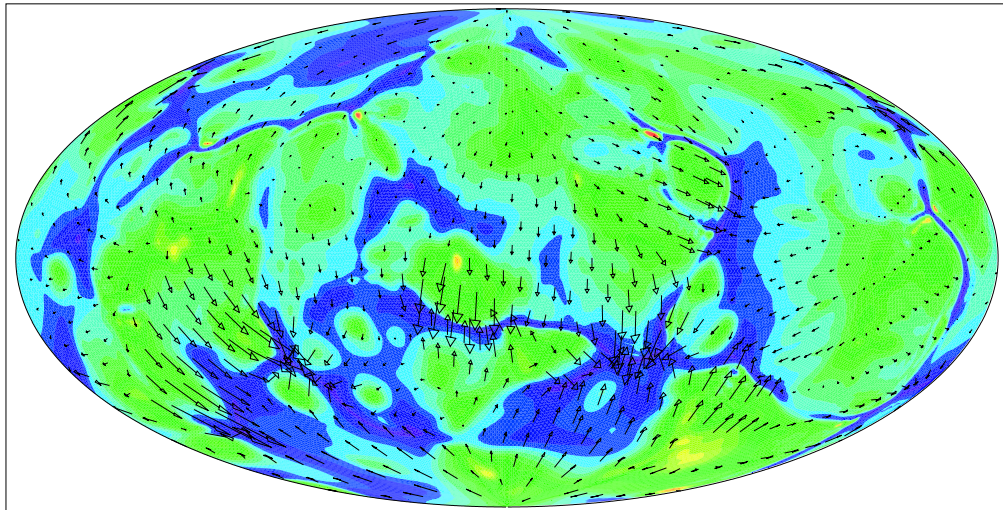
47

Fig. B.2. Equal-area projection of the temperature distribution and creeping velocities (arrows) in 134.8km depth for a yield stress $\sigma_y = 95 GPa$ and a viscosity-level parameter $r_n = +0.4$.

Lauf 618 Y142 man.Staceys   Temperature   3393.
Tcmb Var.3a eta3 ys=1.15e   (K)   2875.
Depth   =   1.348e+02 km   meridian 180° midmost   2358.
Time   =   4.490e+09 a   Age = −2.493e−01 Ma   1840.
Max vel =   3.770e+00 cm/a   Av hor vel =   7.905e−01 cm/a   1323.
                                                                  805.
                                                                  288.

Fig. B.3. Equal-area projection of the temperature distribution and creeping veloc-
ities (arrows) in 134.8km depth for a yield stress $\sigma_y = 115 GPa$ and a viscosity-level
parameter $r_n = -0.4$.

49
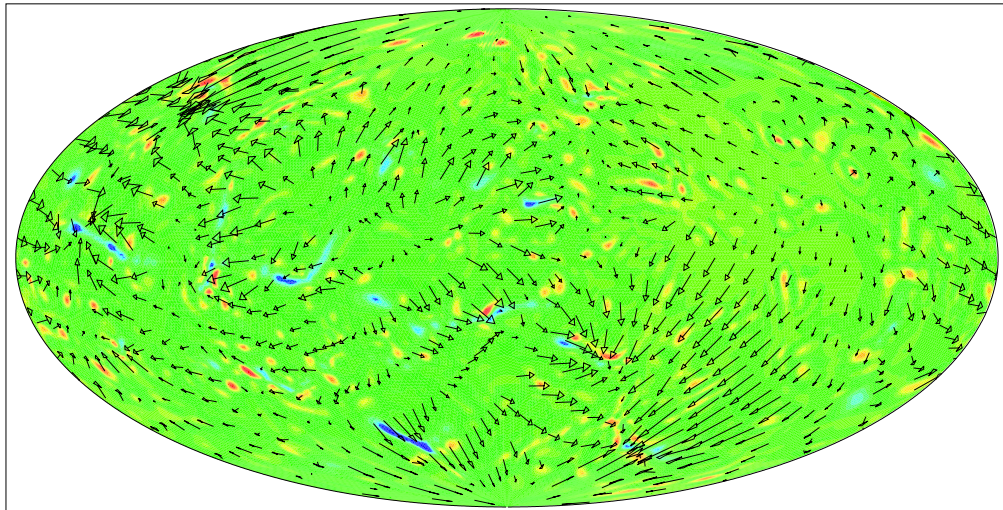
Lauf 546 Y96 man.Staceyst
Tcmb Var.3a eta3 ys=1.8e8
Depth   =   6.329e+02 km
Time   =   4.491e+09 a   Age = −5.668e−01 Ma
Max vel = 2.123e+00 cm/a   Av hor vel =   2.011e−01 cm/a

Temperature
(K)

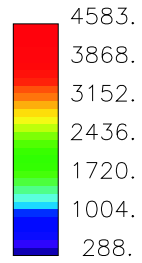4583.
3868.
3152.
2436.
1720.
1004.
 288.

Fig. B.4. Equal-area projection of the temperature distribution and creeping veloc-
ities (arrows) in 632.9km depth for a yield stress $\sigma_y = 180 GPa$ and a viscosity-level
parameter $r_n = -0.5$.